J. Fluid Mech. (2009), *vol.* 638, *pp.* 453–490. © Cambridge University Press 2009
doi:10.1017/S0022112009990693

The finite-length square cylinder near wake

H. F. WANG[1,2,3] AND Y. ZHOU[1]†

[1]Department of Mechanical Engineering, The Hong Kong Polytechnic University,
Hung Hom, Kowloon, Hong Kong

[2]State Key Laboratory of Coal Combustion, Huazhong University of Science and Technology,
Wuhan, People's Republic of China

[3]School of Engineering and Architecture, Central South University, Changsha,
People's Republic of China

(Received 16 June 2008; revised 3 June 2009; accepted 3 June 2009; first published online 5 October 2009)

This paper reports an experimental investigation of the near wake of a finite-length square cylinder, with one end mounted on a flat plate and the other free. The cylinder aspect ratio or height-to-width ratio H/d ranges from 3 to 7. Measurements were carried out mainly in a closed-loop low-speed wind tunnel at a Reynolds number Re_d, based on d and the free-stream velocity of 9300 using hot-wire anemometry, laser Doppler anemometry and particle image velocimetry (PIV). The planar PIV measurements were performed in the three orthogonal planes of the three-dimensional cylinder wake, along with flow visualization conducted simultaneously in two orthogonal planes ($Re_d = 221$). Three types of vortices, i.e. the tip, base and spanwise vortices were observed and the near wake is characterized by the interactions of these vortices. Both flow visualization and two-point correlation point to an inherent connection between the three types of vortices. A model is proposed for the three-dimensional flow structure based on the present measurements, which is distinct from previously proposed models. The instantaneous flow structure around the cylinder is arch-type, regardless of H/d, consisting of two spanwise vortical 'legs', one on each side of the cylinder, and their connection or 'bridge' near the free end. Both tip and base vortices are the streamwise projections of the arch-type structure in the (y, z) plane, associated with the free-end downwash flow and upwash flow from the wall, respectively. Other issues such as the topological characteristics, spatial arrangement and interactions among the vortical structures are also addressed.

1. Introduction

The flow around a nominally two-dimensional cylinder placed normal to a uniform flow has long been the subject of extensive studies, partially because of its importance in engineering and partially because of its highly organized flow structure, facilitating the study of turbulence. This flow is characterized by periodic alternate vortex shedding from the two sides of the cylinder, forming the Kármán vortex street. A large body of knowledge about the two-dimensional cylinder wake has been accumulated (e.g. Oertel 1990; Williamson 1996; Zdravkovich 1997).

In engineering applications, such as pollutant transport around high-rise buildings, plume behaviours behind chimneys, aerodynamic forces on cooling towers or other structures, cylinder-like structures often have a finite length (or height), often with

† Email address for correspondence: mmyzhou@polyu.edu.hk

one end free and the other fixed on the ground. Naturally, these structures cannot be treated as a two-dimensional cylinder. Due to the end effects, the flow structure behind a finite-length cylinder differs drastically from that behind a two-dimensional cylinder, as unveiled in a number of previous investigations, mostly on circular cylinders (e.g. Etzold & Fielder 1976; Kawamura *et al.* 1984; Okamoto & Sunabashiri 1992; Sumner, Heseltine & Dansereau 2004; Adaramola *et al.* 2006; Afgan *et al.* 2007).

The near wake of a wall-mounted finite-length circular cylinder depends strongly on H/d (Sakamoto & Arie 1983; Kawamura *et al.* 1984; Okamoto & Sunabashiri 1992; Summer *et al.* 2004), where H and d are the height and the characteristic width of a cylinder, respectively. When H/d falls below a critical value $(H/d)_{cr}$, vortex shedding changes from the antisymmetrical Kármán type to the symmetric arch-type (Sakamoto & Arie 1983; Okamoto & Sunabashiri 1992; Pattenden, Turnock & Zhang 2005), and the free-end downwash flow dominates the wake. The critical value $(H/d)_{cr}$ is $2 \sim 6$, depending on factors such as the boundary layer thickness and incoming flow turbulence intensity (Sakamoto & Arie 1983; Kawamura *et al.* 1984). For $H/d > (H/d)_{cr}$, alternate Kármán vortex shedding occurs along the cylinder span, except near the free end (Kawamura *et al.* 1984; Okamoto & Sunabashiri 1992), where the influential downwash flow interacts with the Kármán vortices. Ayoub & Karamcheti (1982) reported an intermittence of vortex shedding near the free end. At a relatively large H/d, the free-end effect remains significant over a large portion the cylinder; for example, this effect is appreciable up to $20d$ from the free end for a circular cylinder of $H/d = 30$ (Fox & West 1993*a*,*b*). At $H/d \approx (H/d)_{cr}$, the Kármán-type and arch-type vortices occur intermittently in the near wake. Accordingly, a change occurs in the slope of the St-H/d curves (Sakamoto & Arie 1983).

The wake of a wall-mounted finite-length cylinder is characterized by the presence of the longitudinal tip and base vortices, in addition to possible spanwise Kármán vortex shedding. The interactions between the three types of vortices complicate the flow and make it highly three-dimensional. The tip vortices, associated with the downwash flow from the free end, occur near the free end in the form of a pair of counter-rotating streamwise vortical structures (Etzold & Fiedler 1976; Kawamura *et al.* 1984; Park & Lee 2000). Summer *et al.* (2004) measured the time-averaged cross-stream velocity field behind a wall-mounted finite-length circular cylinder immersed in a boundary layer with a thickness $\delta = 2.6d$, using a 7-hole pressure probe. At $H/d = 5$, 7 and 9, they observed one pair of streamwise vortices near the cylinder base, with the opposite sense to the tip vortices, which are referred to as the base vortices. Both Etzold & Fiedler (1976) and Summer *et al.* (2004) ascribed the formation of the base vortex to the inclined spanwise vortices near the wall. Interestingly, the base vortex is absent when the boundary layer is negligibly thin (Etzold & Fiedler 1976; Okamoto & Sunabashiri 1992; Park & Lee 2000), i.e. the presence of the base vortex depends on the boundary-layer conditions. This is consistent with the finding that the upwash flow induced by the base vortex in a wall-mounted finite-length square cylinder wake is enhanced with the increasing boundary layer thickness (Wang *et al.* 2006).

It is recognized that the flow structure around a wall-mounted finite-length cylinder is much more complicated than that behind a two-dimensional cylinder. Attempts have been made to find a model to describe the flow structure. Based on smoke-wire flow visualization, Etzold & Fiedler (1976) proposed a model in analogy to the flow over a delta wing (refer to figure 11 in Etzold & Fiedler 1976), which consisted of two pairs of streamwise conical vortices, i.e. the tip and base vortices, respectively. However, the structure of spanwise shear flow was not shown in this model. Based on flow visualization and surface pressure distribution measurements,

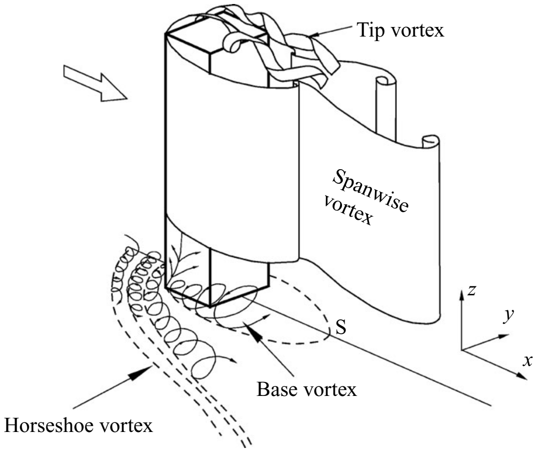

FIGURE 1. Flow structure around wall-mounted finite-length square cylinder with $H/d > (H/d)_{cr}$. (From Wang *et al.* 2005).

Kawamura *et al.* (1984) constituted another model for this flow, and advocated two distinct flow structures, depending on H/d. At $H/d < (H/d)_{cr}$, the near wake was dominated by the streamwise tip vortices; at $H/d > (H/d)_{cr}$, alternate Kármán vortex shedding occurred along most of the cylinder span except near the free end, where the streamwise tip vortices were present (refer to figure 19 in Kawamura *et al.* 1984). Based on previously proposed models and also their own particle image velocimetry (PIV) data, Wang, Zhou & Chan (2005) constructed a model to reflect the interactions between tip, spanwise and base vortices $[H/d > (H/d)_{cr}]$, which is shown in figure 1. Though not identical, the models in Etzold & Fiedler (1976), Kawamura *et al.* (1984) and Wang *et al.* (2005) are essentially similar in representing the tip vortices, showing the stremwise conical vortices separating from the cylinder free end. The filaments of spanwise and tip vortices are not closed in Kawamura *et al.* (1984) model. Tanaka & Murata (1999) observed that the vortex filaments in the wake of a wall-mounted circular cylinder ($H/d = 1.25 \sim 10$), calculated from the measured time-averaged velocities, on both sides of the cylinder were connected with each other near the cylinder free end (refer to figure 9 in Kawamura *et al.* 1984). These filaments displayed an arch-type outlook. They suggested that both tip and base vortices resulted from the projection of the three-dimensional arch-type flow structure in the cross-section plane. It is worth mentioning that the flow structure based on time-averaged velocity measurements may not reflect correctly the details of the instantaneous flow structure. So far it is still debatable whether the tip vortices are isolated from the spanwise vortex roll (Okamoto & Yagita 1973; Etzold & Fiedler 1976; Johnston & Wilson. 1997; Johnston *et al.* 1998; Tanaka & Murata 1999), and there is no consensus on the flow model for the near wake of a wall-mounted finite-length cylinder.

This work aims to investigate experimentally the flow around a wall-mounted finite-length square cylinder in order to gain a better understanding of the near wake, in particular, the interrelationship among the tip, base and spanwise vortices. An obvious advantage from investigating the square cylinder rather than the circular is that the flow separation is fixed at the leading edge, thus simplifying the problem concerned. The PIV measurements were conducted in three orthogonal plans, along with flow visualization performed simultaneously in two orthogonal planes in order to capture the three-dimensional aspects of the flow structure. The H/d range examined is $3 \sim 11$, with a detailed discussion around $H/d = 3 \sim 7$ which is typical for many engineering structures such as the tall buildings in Hong Kong.

2. Experimental details

2.1. *Wind tunnel and test model*

Experiments were conducted in a closed-loop low-speed wind tunnel with a 2.4 m long test section of $0.6\,\text{m} \times 0.6\,\text{m}$. The flow velocity in the test section was uniform to 0.1 % and the longitudinal turbulence intensity was less than 0.4 %. See Huang, Zhou & Zhou (2006) for more details of the tunnel. A square cylinder was mounted on the upper surface of a horizontal flat plate to generate the wake. Figure 2(*a*) shows the schematic of experimental set-up and the definition of the coordinate system. The plate of 0.5 m in width and 1.2 m in length was 10 mm thick, with a carefully rounded leading edge to avoid flow separation. Its upper surface was 0.15 m from the bottom wall of the test section to eliminate the possible effects of the boundary layer over the test section wall. The square cylinder with a width $d = 20\,\text{mm}$ was placed at the centreline, 0.3 m downstream of the leading edge of the flat plate. The H/d investigated was $3 \sim 11$. The blockage ratio was 3 %, smaller than the threshold (5 %) suggested by Farell *et al.* (1977), thus resulting in a negligibly small blockage effect. All measurements were conducted at a free-stream velocity $U_\infty = 7\,\text{m}\,\text{s}^{-1}$, corresponding to a Reynolds number $Re_d \equiv U_\infty d/\nu = 9300$, where ν is the kinematic viscosity of fluid. A two-component laser Doppler anemometer (LDA) was used to document the boundary layer, developed over the flat plate, at the cylinder axis. Figure 3 presents the time-averaged streamwise velocity ($\overline{U^*}$) and root mean square (r.m.s.) value of streamwise fluctuation velocity (u^*_{rms}) measured in the absence of the cylinder, where the overbar denotes conventional time averaging and an asterisk represents normalization by U_∞ and/or d. The boundary layer disturbance thickness (δ) was estimated to be 27 mm so that $\delta/d \approx 1.35$, and the boundary layer displacement thickness (δ_1) was 6.6 mm. The boundary layer thickness may have a pronounced influence on the flow structure around a wall-mounted finite-length cylinder. Wang *et al.* (2006) noted a significant upwash flow at $\delta/d \approx 1.02$ ($Re_d = 11\,500$), which was linked with the occurrence of the base vortex. The upwash flow was enhanced with increasing boundary layer thickness.

2.2. *LDA measurements*

All LDA, PIV and hotwire measurements were conducted in the wind tunnel described in § 2.1. In order to obtain quantitative information of the flow field at a close vicinity downstream of the cylinder, a two-component LDA system (Dantec Model 58N40 with enhanced FVA signal processor) was used to measure velocities in the (x, z) plane at $y^* = 0$. The laser source was an argon ion laser (Spectra-Physics, Stabilite 2017) with a maximum power output of 4 W. The measuring volume has a minor axis of 1.18 mm and a major axis of 2.48 mm. The LDA optic probe was mounted on a computer-controlled traversing system with a maximal positional error of ± 0.06 mm. The flow was seeded by smoke generated from paraffin oil by a smoke generator. The averaged seeding particle diameter was about 1 μm. The number of samples collected at each measurement point was 5000 for both U and W, with a typical validation rate of 80 % ∼ 90 %. The LDA system comes with the necessary software for data processing and analysis to produce the time-averaged velocities and Reynolds stresses. The uncertainty of LDA measurements consists of precision and bias uncertainty, viz.

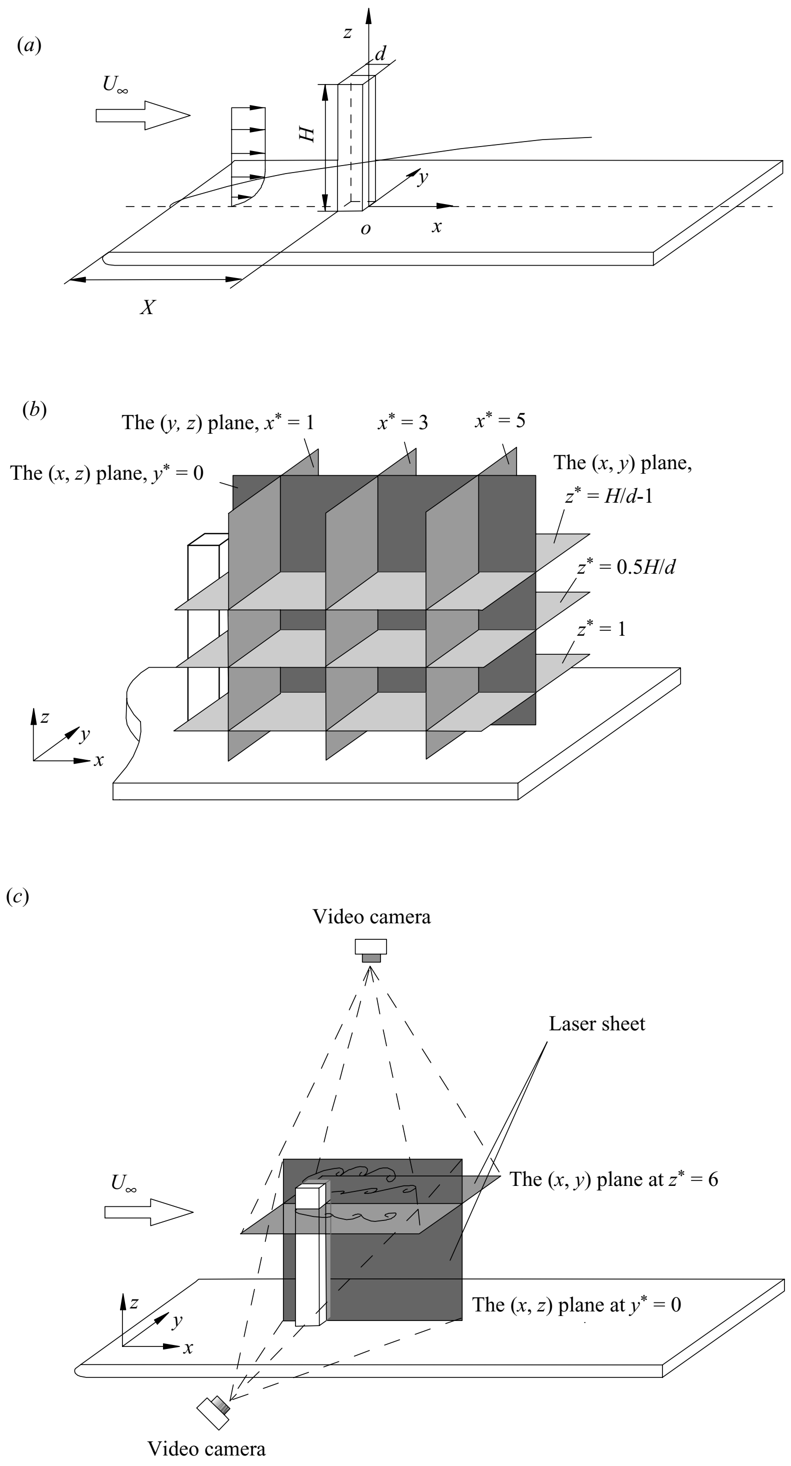

FIGURE 2. (*a*) Schematic of experimental set-up and the definition of the coordinate system, (*b*) experimental PIV measurement planes and (*c*) arrangement of flow visualization simultaneously in two orthogonal planes.

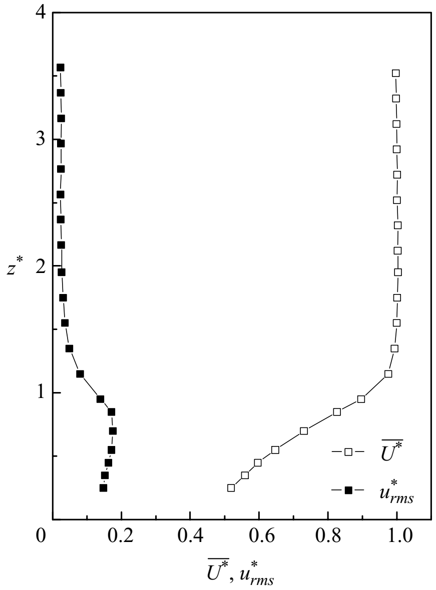

FIGURE 3. Distributions of the time-averaged and rootmean square streamwise velocity, i.e. $\overline{U^*}$and u^*_{rms}, measured at the cylinder axis. Measurements were performed in the absence of cylinder.

$U_{total} = \pm(B + tP)$, where B is the bias uncertainty, P is the precision uncertainty and $t = 1.96$ for a 95 % confidence level (for a sample size greater than 50) (Kunz *et al.* 2001). The bias uncertainty is very small, compared to the precision uncertainty, and may be neglected. The uncertainty in present LDA measurements results largely from averaging a finite number of data samples at each measurement point. The sampled velocity does not remain constant but fluctuates due to turbulence. Assuming a normal distribution in velocity samples, the precision error in the time-averaged velocity is then $1/\sqrt{N}(v_{rms}/\overline{V})$, where $(v_{rms}/\overline{V})$ is the local turbulent intensity. Given a sample size greater than 50, the uncertainty from the precision error can be estimated by $1/\sqrt{2N}$ (Patterson 1982). As such, the uncertainty is presently estimated to be about 1 % in the time-averaged velocities and the error propagation of the measured velocities indicates a 4 % uncertainty in the Reynolds stresses.

2.3. *Hotwire measurements*

A hotwire, operated on a constant temperature circuit at an overheat ratio of 1.6, was deployed to measure streamwise fluctuating velocity u in order to determine the vortex-shedding frequency. Its sensing element was made of 5 μm tungsten wire approximately 1.5 mm in length. The hotwire was traversed along the spanwise direction at $y^* = 2$ and $x^* = 3$, 5 and 10. The signal from the wire was offset, low-pass filtered at a cutoff frequency of 1.5 kHz, and then sampled at a frequency of 3 kHz. The sampling duration for each record was 20 s. The frequency resolution Δf in the spectral analysis depends on the sampling frequency and window size of fast Fourier transform used. The present Δf is estimated to be about ± 0.86 Hz, thus yielding an experimental uncertainty in St ($\equiv f_s \cdot d/U_\infty$, where f_s is the vortex shedding frequency) of 2.3 %.

In order to measure the spanwise correlation of flow, two hotwires were placed at $y^* = 2$ and $x^* = 3$, with one fixed at $z^* = 1$ and the other traversed along the cylinder span at an increment of 1*d*. The signals from the two wires were recorded simultaneously at the same sampling conditions as those used in the single hotwire measurements.

2.4. *PIV measurements*

A DANTEC standard PIV2100 system was used to measure both the instantaneous and time-averaged flow fields. The flow was seeded by the same smoke as used in the LDV measurements. Flow illumination was provided by two New Wave standard pulse laser sources of a 532 nm wavelength, each with a maximum energy output of 120 mJ pulse^{-1}. Each laser pulse lasted for 0.01 μs. Particle images were taken using one CCD camera (HiSense type 13, gain × 4, double frames, 1280 × 1024 pixels). Synchronization between image taking and flow illumination was provided by the Dantec FlowMap Processor (PIV2001 type).

PIV measurements were performed in the (x, z) plane ($y^* = 0$), three (x, y) planes ($z^* = 1$, $0.5\,H/d$ and $H/d - 1$) and three (y, z) planes ($x^* = 1$, 3, 5), as shown in figure 2(*b*). The image magnifications in the (x, z), (x, y) and (y, z) planes are 148, 153 and 157 μm pixel^{-1}, respectively. The interval between two successive pulses was 50 μs for measurements in the (x, z) and (x, y) planes. Thus, a particle would travel longitudinally only about 0.35 mm (0.018*d*) at $U_\infty = 7.0\,\mathrm{m\ s^{-1}}$. For measurements in the (y, z) plane, where v and w were obtained, the CCD camera was placed on the flat plate inside the wind tunnel, about 50*d* downstream from the cylinder to minimize any possible disturbance to the flow of concern. Since the main stream is normal to the (y, z) plane, the out-of-plane component of velocity is relatively large compared to the measurements in the other two planes, that is, the tracing particles could cross the light sheet given a large time interval between two successive images used in determining velocity vectors, thus resulting in poor correlation (Pattenden *et al.* 2005). In the present measurement, this time interval was set to 10 μs, which was found to produce satisfactory results. Since the cylinder appeared in the PIV images, erroneous velocity vectors might occur due to the reflection noise from the cylinder. Such vectors have been removed using a built-in range validation function, and then replaced with interpolated values from eight surrounding data points. In order to examine the streamwise evolution of the near-wake longitudinal structures, measurements were performed in the (y, z) planes at $x^* = 1$, 3 and 5, respectively.

In processing PIV images, an interrogation areas of 32 × 32 pixels were used with a 50 % overlap in both directions, producing 78 × 62 in-plane velocity vectors and the same number of vorticity data (ω_x, ω_y or ω_z). The vorticity data was calculated by a built-in function of the FlowMap Processor (PIV2001 type) based on eight surrounding velocity data. The spatial resolution of vorticity data was about 4.7 mm, 4.9 mm and 5.0 mm or 0.24*d*, 0.25*d* and 0.25*d* in the (x, z), (x, y) and (y, z) planes, respectively. This resolution may considerably degrade the vorticity estimate in view of the Kolmogorov length scale, estimated presently to be in the order of 0.1 mm. On the other hand, the integral length scale of the wake flow is in the order of cylinder width d, i.e. 20 mm, suggesting that the spatial resolution for vorticity is adequate in capturing the large-scale vortical structures, which are of the primary interest presently. A total of 1500 PIV images were captured to calculate time-averaged velocities and Reynolds stresses in the (x, y) plane, and 200 images were captured to calculate time-averaged sectional streamlines and vorticity contours in the (x, z) or (y, z) plane.

The present flow is highly three-dimensional, and the out-of-plane velocity component may introduce an error in the in-plane velocity measurement because of the perspective projection effects (Raffel, Willert & Kompenhans 1998). One way to avoid this error is to measure all three components of the velocity vectors, for example by means of stereoscopic PIV (SPIV) techniques. Fouras, Dusting & Hourigan (2007) and Fouras, Jacono & Hourigan (2008) proposed a target-free SPIV calibration technique. No interpolation process is required, and the calibration automatically takes into account any discrepancy between two camera images, thus reducing the sensitivity to camera misalignments, lens misalignments and magnification differences. In present two-dimensional PIV measurements, the camera lens axis is perpendicular to the laser-illuminated measurement plane. The error due to the perspective projection of the out-of-plane velocity into the measurement plane is linked to the effective view angle of the image and is relatively large at the edges of the image field (Lourenço *et al.* 1986). The effective view angle of the present 50 mm lens CCD camera is about 26.5°. With the out-of-plane velocity magnitude considered, the perspective projection effect may cause an error in velocity measurement of about 8 % at the edge of the image field and less than 4 % in the central region. Most flow structures of the present concern are located near the centre of the image. (e.g. see figure 5). Raffel *et al.* (1998) suggested that this systematic effect could be treated as random errors and should not hamper the interpretation of the instantaneous flow field. Therefore, the prospective projection effect caused by the out-of-plane velocity component is not considered in this investigation.

2.5. *Laser-induced fluorescence flow visualization*

Flow visualization was conducted using the LIF technique (Williamson 1988) in a water tunnel with a 2.4 m long test section and a cross-section of $0.3\,\mathrm{m} \times 0.6\,\mathrm{m}$. The flow velocity in the test section ranges from $0.01\,\mathrm{m\,s^{-1}}$ to about $4\,\mathrm{m\,s^{-1}}$. The tunnel was described in detail by Wang *et al.* (2006). The cylinder installation was similar to that in the wind tunnel. A 10 mm thick flat plate of 0.3 m in width and 1 m in length was horizontally installed in the water tunnel. Its upper surface is 0.15 m from the bottom wall of the test section. The leading edge of the plate was rounded carefully to avoid flow separation. A square cylinder of $d = 20$ mm was mounted at the centreline of the plate, 0.2 m downstream of the leading edge. The H/d ratios were the same as used in the wind tunnel measurements. The blockage ratio was 6.7 %. The free-stream velocity for flow visualization is $0.01\,\mathrm{m\,s^{-1}}$ and the corresponding Re_d is 221.

To mark the flow, dye (Rhodamine 6G 99 %), which has a faint red colour and emits a metallic green when excited by laser of 488 nm wavelength, was introduced into the flow through pinholes of 0.5 mm in diameter located symmetrically on the vertical leading edges of the cylinder at $z^* = 1$, 3.5 and 6. Another injection pinhole was made at the centre of the free-end leading edge to mark the free-end shear flow.

Given a highly three-dimensional wake, flow visualization was carried out in the (x, y) plane at $z^* = 1$, 3.5 and 6 for $H/d = 7$. Flow visualization was also performed simultaneously in two orthogonal planes (figure 2*c*), i.e. the (x, y) plane at $z^* = 6$ and the (x, z) plane at $y^* = 0$, in order to capture the three-dimensional aspects of vortical structures emanating from the free end, including interaction between the free-end and spanwise shear layers. The two planes were simultaneously illuminated by two laser sheets generated by two identical laser sources (Spectra-Physics, Stabilite 2017) with a maximum output power of 4 W. Two identical digital video cameras (SONY, DCR-PC100E) were used, and their operations were synchronized using a single remote controller, thus ensuring the simultaneous capture of images in the two planes.

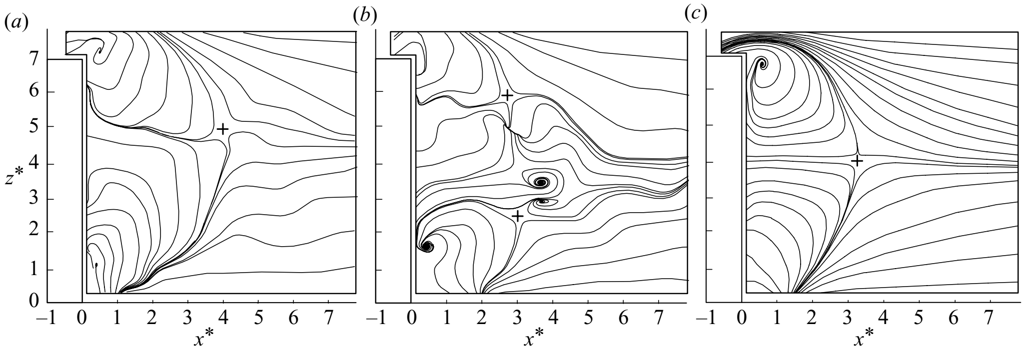

FIGURE 4. Typical instantaneous (*a*, *b*) and time-averaged (*c*) sectional streamlines in the (*x*, *z*) plane at $y^* = 0$, viewed on a fixed reference frame. $H/d = 7$. Saddles are denoted by '+'.

3. The flow structure

3.1. *Downwash and upwash motion*

This section is focused on the flow structure at $H/d = 7$. Figure 4 shows typical instantaneous and time-averaged sectional streamlines in the (*x*, *z*) plane at $y^* = 0$. The sectional streamlines are viewed from a reference frame fixed on the cylinder, and will be hereinafter referred to as streamlines for simplicity. Two distinct types of typical instantaneous streamlines have been observed. One is characterized by free-end downwash flow meeting with upwash flow from the wall, and the downwash flow is limited to the upper half of the wake (figure 4*a*). The saddle point, marked by the symbol '+', in the figure results apparently from interaction between upwash and downwash flows. The other appears more complicated, showing more critical points (e.g. Zhou & Antonia 1994), including two saddle points, three foci and a node (figure 4*b*). The presence of two foci associated with counter-rotating vortical structures is consistent with the occurrence of mushroom-like longitudinal rib structures, as observed by Wu *et al.* (1994, 1996) in close proximity to the cylinder. Wu *et al.* (1994, 1996) used a cylinder of $H/d = 26$ or 38, much larger than the present H/d ($= 7$). Accordingly, their vortex rolls should be much longer. This explains why many mushroom-like rib structures were seen in their flow visualization, but only two counter-rotating foci occurred in figure 4(*b*). These rib structures are inherently associated with spanwise vortex rolls (Wu *et al.* 1994, 1996), i.e. the flow topology in figure 4(*b*) is linked to the occurrence of spanwise vortex shedding. On the other hand, the predominance of downwash and upwash flows shown in figure 4(*a*) corresponds to the absence of spanwise vortex shedding at this instant. The flow about the node is strongly three-dimensional, with a large velocity gradient in the *y* direction (Zhou & Antonia 1994). The presence of the node is ascribed to the rollup of spanwise shear layer that sweeps across the central plane ($y^* = 0$). The two saddle points probably result from the interaction between upwash or downwash flow and spanwise shear flow. Time-averaged streamlines (figure 4*c*) out of 200 instantaneous images are topologically similar to those in figure 4(*a*), and also to those behind a wall-mounted finite-length circular cylinder of the same H/d (Sumner *et al.* 2004). This is not unexpected. The rib structures and hence the foci in figure 4(*b*) occur rather randomly in time and also in the streamwise and spanwise locations. So does the node. Consequently, these critical points have been averaged out (figure 4*c*).

3.2. *Spanwise structure*

The flow behind a wall-mounted finite-length cylinder is highly three-dimensional, varying remarkably along the cylinder span. Figure 5 presents typical instantaneous ω_z^* contours in three (x, y) planes at $z^* = 1$, 3.5 and 6 $(H/d = 7)$. The reverse flow occurs in immediate proximity to the cylinder. The boundary of the time-averaged reverse flow zone, determined from $\overline{U^*} = 0$ in the (x, y) or (x, z) plane, is marked by a thick solid line to facilitate data interpretation. As expected, the streamwise extent of this zone depends on z^*, largest at mid-span $(z^* = 3.5)$ and smallest near the free end $(z^* = 6)$, similarly to previous observations behind a wall-mounted finite-length circular cylinder (Okamoto & Sunabashiri 1992; Sumner *et al.* 2004). The small size near the free end is apparently linked to the rolling down free-end shear flow (figure 4*c*), which acts to suppress spanwise vortex shedding (Farivar 1981; Okamoto & Sunabashiri 1992). Similarly, the reduced size near the wall, though larger than near the free end, is ascribed to the upwash flow from the wall (figure 4*c*), which is also inclined to weakening spanwise vortices (Wang *et al.* 2006).

Sakamoto & Arie (1983) proposed two major types of near-wake spanwise vortices, i.e. antisymmetric Kármán-type vortices and symmetric arch-type vortices behind a wall-mounted finite-length circular cylinder $(H/d = 1 \sim 8$, $Re_d = 270 \sim 920)$. They further suggested a predominance by the former at $H/d > (H/d)_{cr}$ and by the latter at $H/d < (H/d)_{cr}$. At $H/d \approx (H/d)_{cr}$, both types of vortices were observed intermittently. $(H/d)_{cr}$ was estimated to be 2.5 and 3 for circular and square cylinders, respectively. It is worth mentioning that the results of Sakamoto and Arie (1983) were based on flow visualization only at mid-span for each H/d. Okamoto & Sunabashiri (1992) examined the dependence of spanwise vortices on the spanwise position in the wake of a wall-mounted finite-length circular cylinder $(H/d = 7$, $Re_d = 1060)$ and noted that the Kármán-type vortices occurred along most of the cylinder span except near the free end, where the vortices were symmetrically arranged under the effects of downwash flow. In the wake of a wall-mounted finite-length square cylinder $(H/d = 5)$, however, Wang *et al.* (2006) observed from the PIV measurements both antisymmetrically and symmetrically arranged vortices throughout the cylinder span, thus advocating that, while Kármán-type vortex shedding was antisymmetric, both downwash flow from the free end and upwash flow from the wall acted to alter vortex shedding from the antisymmetric to symmetric arrangement. Naturally, the symmetric arrangement occurred more frequently near the free end and wall.

It could be interesting to examine the configurations of spanwise vortices at different z^* at $H/d = 7$, which exceeds considerably $(H/d)_{cr} = 3$ (Sakamoto & Arie 1983). The Q-criterion (Hunt, Wray & Moin 1998) is used to identify the vortex centres from the PIV-measured instantaneous velocity data, which is essentially similar to the critical-point technique (Perry & Chong 1987; Zhou & Antonia 1994). Readers may refer to Hunt *et al.* (1998) and Jeong & Hussain (1995) for the detailed description of this method. Briefly, the criterion Q is defined as

$$Q = \frac{1}{2}(r_{ij}r_{ij} - s_{ij}s_{ij}), \tag{3.1}$$

where s_{ij} and r_{ij} are the symmetrical strain tensor and skew-symmetrical rotation tensor, viz.

$$s_{ij} = \frac{1}{2}\left(\frac{\partial u_i}{\partial x_j} + \frac{\partial u_j}{\partial x_i}\right), \tag{3.2}$$

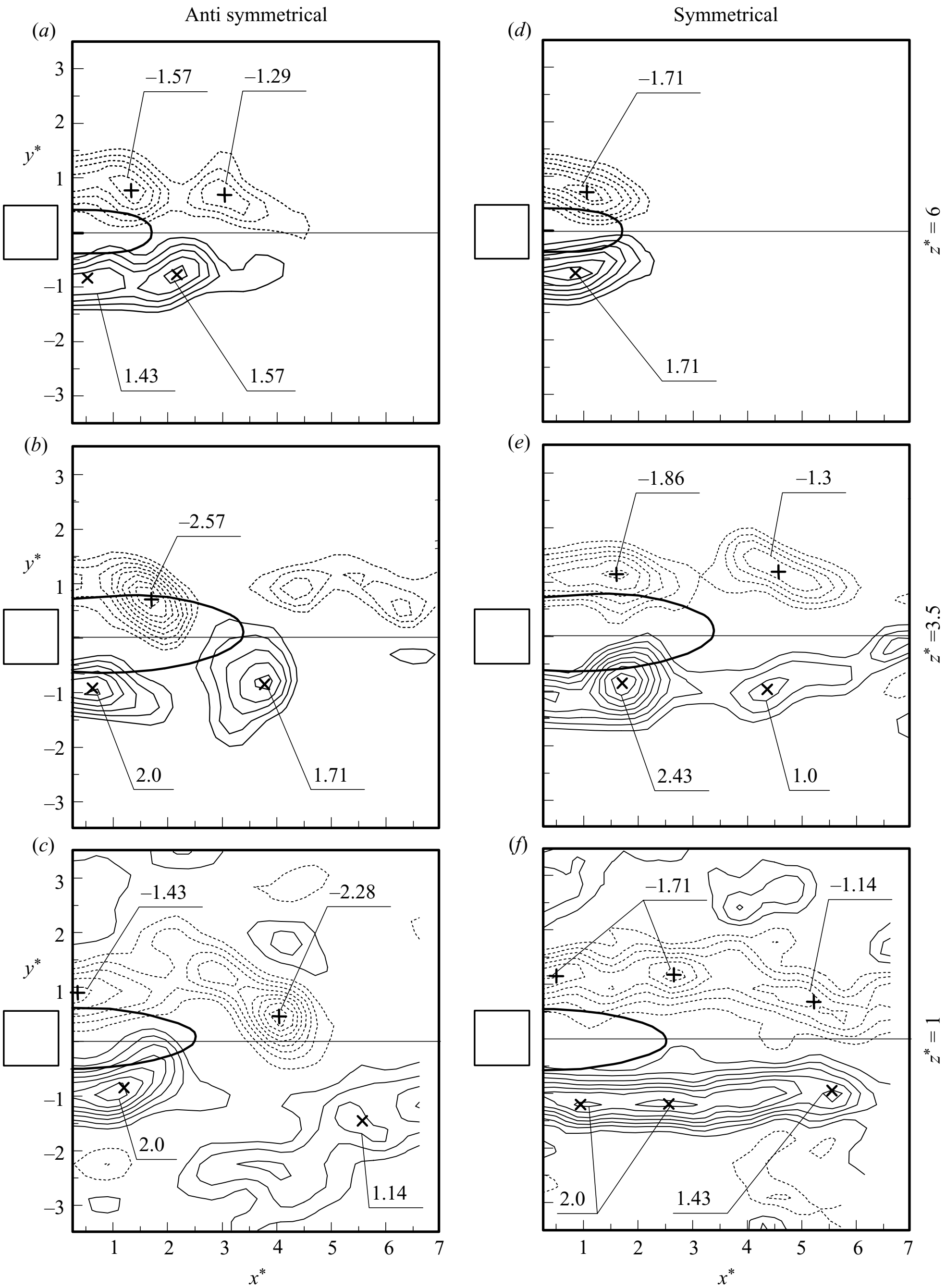

FIGURE 5. Instantaneous ω_z^* contours of antisymmetrically arranged vortices (*a–c*) and symmetrically arranged vortices (*d–f*), $H/d = 7$. The symbols '×' and '+' mark the vortex centres of positive and negative vorticity concentrations, respectively. (*a*, *d*) $z^* = 6$, $\Delta\omega_z^* = 0.14$; (*b*, *e*) 3.5, 0.28 and (*c*, *f*) 1, 0.28. The bold line denotes the boundary of reverse flow zone, determined by $\overline{U^*} = 0$. The square to the left of each plot indicates the location of the cylinder.

$$r_{ij} = \frac{1}{2}\left(\frac{\partial u_i}{\partial x_j} - \frac{\partial u_j}{\partial x_i}\right), \tag{3.3}$$

where i, $j = 1, 2$ and 3; u_1, u_2 and u_3 are the velocity components along the x_1, x_2 and x_3 directions of the Cartesian coordinate system, respectively. Q is calculated from instantaneous two-dimensional velocity data based on (3.1)–(3.3). A vortex is detected once the condition $Q = kQ_m$ is satisfied, where Q_m is the maximum Q in each PIV-measured instantaneous velocity field and $k = 0.7$ is a threshold. This threshold is chosen to ensure the detection of only large-scale vortical structures, based on visually comparing detected vortices with the PIV-measured ω_z contours. The small-scale vortical structures, e.g. the structure at $(x^*, y^*) = (4.5, 0.9)$ in figure 5(*b*) and the one at $(x^*, y^*) = (3.8, 2.5)$ in figure 5(*f*), will not be detected, which are not of interest here. The location, where a local maximum Q occurs, is identified as the vortex centre. The centres associated with negatively and positively signed vorticity concentrations are marked by '+' and '×', respectively, as illustrated in figure 5. Note that the full local gradient tensor cannot be determined from two-dimensional PIV measurements. Using a two-dimensional Q-criterion technique, Zhong, Huang & Adrian (1998) and Adrian, Christensen & Liu (2000) successfully identified vortices from planar PIV data in a channel and a pipe flow, respectively. This is indeed reconfirmed presently and the identified vortex centres coincide well with those of the local peaks of ω_z, as is evident in figure 5.

Both symmetrically and antisymmetrically arranged spanwise vortices are observed at $z^* = 1$, 3.5 and 6, as illustrated in figure 5, reconfirming Wang *et al.*'s observation at $H/d = 5$ and $Re_d = 11\,500$ (Wang *et al.* 2006). Near the free end ($z^* = 6$), spanwise vortices, especially symmetrically arranged (figure 5*d*), are invisible beyond a small longitudinal distance behind the cylinder under the influence of the free end downwash flow. Alternate spanwise vortex shedding is also observed in figure 5(*a*). This configuration of vortices is evident at the cylinder mid-span (figure 5*b*). These alternately shed vortices do not appear to survive long, probably linked to the three-dimensional nature of the flow. Interestingly, symmetric vortex shedding also occurs at mid-span (figure 4*e*), though infrequently. At $z^* = 1$, the flow structure appears more complex probably due to interactions between the near wake and the boundary layer (note that $\delta^* \approx 1.35 > z^* = 1$). Again, the two types of vortical structures are discernable (figure 5*c*,*f*).

3.3. *Tip and base vortices*

Figure 6 shows typical instantaneous cross-stream velocity vectors in the (y, z) plane and the corresponding ω_x^* contours measured at $x^* = 5$. The flow structures measured at $x^* = 1$ and 3 are topologically similar to their counterparts at $x^* = 5$, and thus not shown. Two distinct flow patterns are observed, which occur intermittently. One is illustrated in figure 6(*a*, *b*), when spanwise shear flow sweeps across the central plane, i.e. the (x, z) plane at $y^* = 0$. Vortical structures, which are probably the signature of longitudinal vortices in the (y, z) plane, cannot be observed on the right-hand side of the cylinder; the alternatively signed ω_x^* concentrations occur on the left-hand side of the cylinder (figure 6*b*), similarly to the rib structures observed in a two-dimensional cylinder wake (Chyu & Rockwell 1996; Wu *et al.* 1996; Huang *et al.* 2006). It may be inferred that the flow pattern shown in figure 6(*a*, *b*) corresponds to the rollup of spanwise shear layer sweeping across the central plane, over most of the cylinder span. The other flow pattern, shown in figure 6(*c*, *d*), is characterized by two pairs of counter-rotating vortical structures, one pair near the free end of the cylinder and

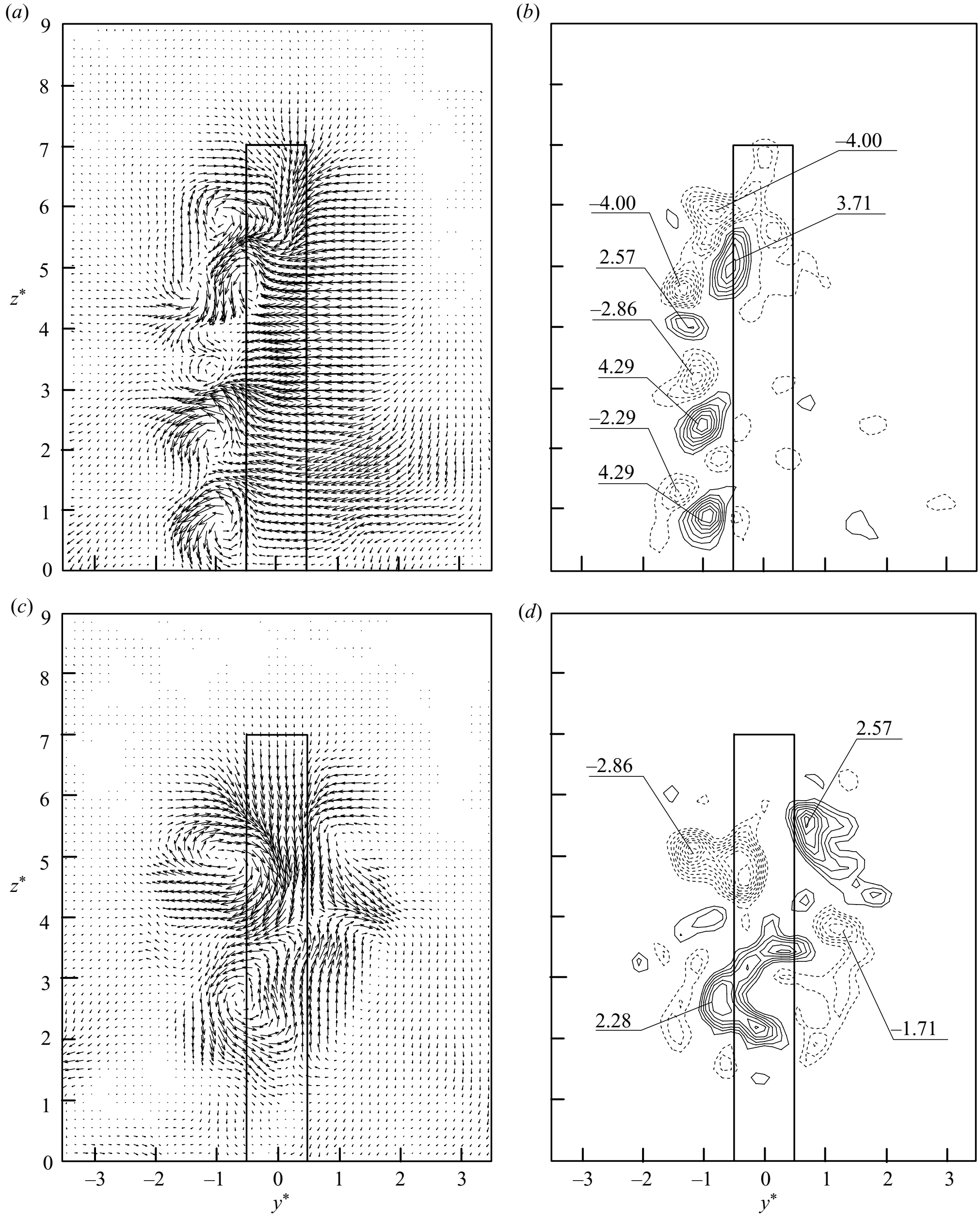

FIGURE 6. Typical instantaneous velocity vectors and corresponding ω_x^* contours in the (y, z) plane at $x^* = 5$, $H/d = 7$. (*b*) $\Delta\omega_x^* = 0.51$, (*d*) 0.28. (*a*, *b*) spanwise shear flow sweeps across the central plane and dominates the wake, longitudinal 'mushroom' vortical structure presents in (*b*). (*c*, *d*) spanwise shear flow retreats, downwash and upwash flow dominate the wake, tip vortices and base vortices present symmetrically in (*d*).

the other near the wall. The former is linked to the downwash flow emanating from the free end and the latter is connected to the upwash flow from the base, referred to presently as the 'tip vortices' and 'base vortices', respectively. As evident in figure 6(*c*), the upwash and downwash flow dominate, clashing with each other near the mid span

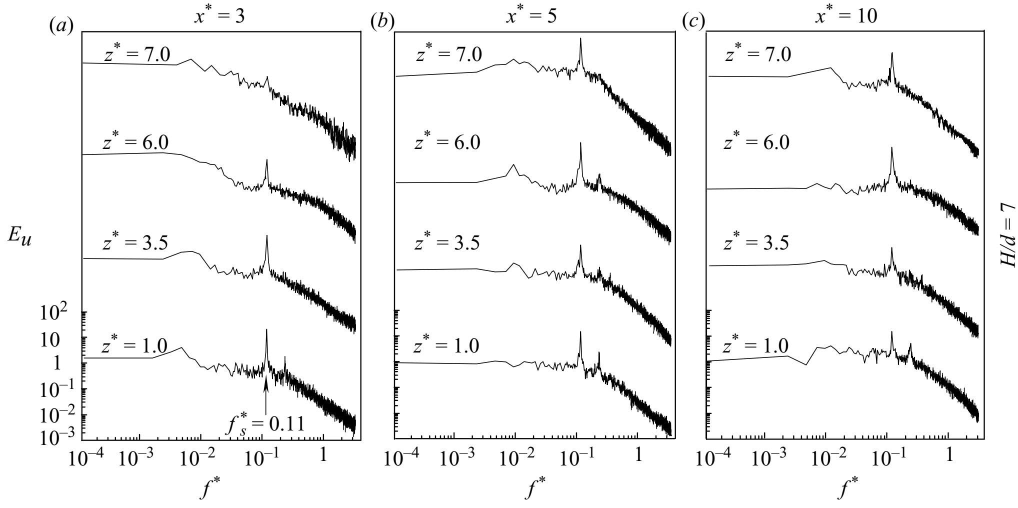

FIGURE 7. The power spectral density function E_u of the streamwise fluctuating velocity u at $y^* = 2$, $H/d = 7$. (*a*) $x^* = 3$, (*b*) = 5, (*c*) 10.

of the cylinder, without the signature of the spanwise vortices throughout the entire cylinder span. The longitudinal tip or base vortex pair is symmetrically arranged about the cylinder (figure 6*d*). It is worth pointing out that the upwash flow and base vortices cannot be ascribed to the horseshoe vortex formed around the cylinder base (Sumner *et al.* 2004). The horseshoe vortex is characterized by a rollup motion in front of the obstacle, wrapping around its two sides and then trailing off behind, and tends to drive flow downwards inside its vertical tails (Hussein & Martinuzzi 1996; Simpson 2001).

The two distinct flow patterns captured in the (y, z) plane (figure 6) are related with the two types of flow structures observed in the (x, z) and the (x, y) plane (figures 4 and 5). During Kármán vortex shedding, the spanwise shear layer rolling and sweeping across the central plane (e.g. figure 5*b*) is probably responsible for the presence of the node and foci in the central plane (figure 4*b*). The corresponding spanwise vortices are naturally antisymmetrically arranged (figure 5*b*). In view of the association between Kármán vortices and rib structures (e.g. Wei & Smith 1986; Wu *et al.* 1996), the alternately signed ω_x^* concentrations, which are the signature of the longitudinal rib structures in the (y, z) plane, occur only on one side of the cylinder (figure 6*b*). On the other hand, in the absence of spanwise Kármán vortex shedding, no shear layer sweeps across the central plane and the node and the counter-rotating foci could not be seen (figure 4*a*). Instead, the downwash and upwash flows are predominant in the near wake and clash with each other (figure 6*c*), resulting in symmetrically arranged spanwise vortices in some (x, y) planes (figure 5*d–f*), if not all, and spontaneously the simultaneous occurrence of tip and base vortex pairs, each symmetrically arranged about the cylinder.

3.4. *Quasi-periodical flow structure and its spanwise coherence*

Figure 7 presents the power spectral density function E_u of streamwise fluctuating velocity u measured using a hotwire at different spanwise locations for various x^*. The ordinate scale is arbitrary in figure 7, though the same scale is used for every spectrum for the purpose of comparison. In close proximity to the cylinder ($x^* = 3$), E_u

measured at mid span ($z^* = 3.5$) displays a pronounced peak at $f_s^* = 0.11$ (figure 7*a*), indicating the occurrence of spanwise vortex shedding. This dominant frequency is lower than that in a two-dimensional square cylinder wake, which was $0.125 \sim 0.13$ for $Re_d = 1 \times 10^3 \sim 2 \times 10^4$ (e.g. Okajima 1982). A similar observation was made in a finite-length circular cylinder wake (Sakamoto & Arie 1983; Sumner *et al.* 2004). Zdravkovich (2003) ascribed the decrease in the Strouhal number in the finite-length cylinder wake to the free-end downwash flow and suggested that the downwash flow elongate the vortex formation length and widen the near wake, thus prolonging spanwise vortex shedding.

The Strouhal number measured at other spanwise locations is identical to that at mid span. A minor peak occurs at $f^* = 0.22$ in E_u at $z^* = 1$, apparently due to the second harmonic of f_s^*. This peak is also discernible at $z^* = 3.5$. The major peak of the u-spectrum appears weak at $z^* = 7$, resembling the observation in a finite-length circular cylinder wake (Sumner *et al.* 2004) because the downwash flow interacts with and hence weakens spanwise vortex shedding (Okamoto & Sunabashiri 1992). Further downstream at $x^* = 5$ and 10, a pronounced peak occurs at $f^* = 0.11$ for all spanwise locations, including $z^* = 7$ (figure 7*b*,*c*), suggesting a weakened downwash flow effect. The fact that the major peak in E_u occurs at the same frequency throughout the cylinder span implies that the tip and base vortices may separate from the cylinder at the same frequency as spanwise vortices, and each of the three types of vortices may be part of the same entity of the organized structure.

To understand better the near wake structure, two-point hotwire measurements were performed at $x^* = 3$, with one wire fixed at $y^* = 2$ and $z^* = 1$ and the other at the same y^* and traversed along the cylinder span, producing two hotwire signals u_1 and u_2, respectively. The spectral coherence $Coh_{u_1u_2} = (Co_{u_1u_2}^2 + Q_{u_1u_2}^2)/E_{u_1}E_{u_2}$ between u_1 and u_2 provides a measure of the degree of correlation between the Fourier components of u_1 and u_2, where $Co_{u_1u_2}$ and $Q_{u_1u_2}$ are the cospectrum and quadrature spectrum of u_1 and u_2. $Coh_{u_1u_2}$ exhibits a pronounced peak at $f^* = 0.11$ at all spanwise locations (figure 8). The peak value of $Coh_{u_1u_2}$ranges from more than 0.9 at $z^* = 2$ to about 0.3 at $z^* = 7$, suggesting a significant spanwise correlation between vortex separation throughout the cylinder span, and thus corroborating that the tip, spanwise and base vortices may each be considered as part of one single vortical structure.

In a two-dimensional cylinder wake, vortices are highly coherent in the spanwise direction. The phase lag at f_s between the lateral fluctuating velocity signals (v) is approximately zero across the wake (Zhou, Zhang & Liu 2002). The present case may be different due to the presence of the free-end downwash flow and the boundary layer over the wall. Figure 9 shows the spectral phase angle, $\phi_{u_1u_2}(\equiv \tan^{-1}(Q_{u_1u_2}/Co_{u_1u_2}))$, between simultaneously measured u_1 and u_2 at $z^* = 1$ and 2, which provides the information on the averaged phase shift between the spectral components of u_1 and u_2. A plateau occurs in $\phi_{u_1u_2}$ at about $f_s^* = 0.11$, where $\phi_{u_1u_2} \approx 0.02\pi$, indicating that the vortex separation at $z^* = 2$ leads that at $z^* = 1$ by 0.02π. Figure 10 presents the dependence of $\phi_{u_1u_2}$at $f_s^* = 0.11$ on z^*. There is no plateau in $\phi_{u_1u_2}$at $f_s^* = 0.11$ for $z^* = 7$, probably because of a very low spectral coherence between u_1 measured at $z^* = 1$ and u_2 at $z^* = 7$. Therefore, no data is shown at $z^* = 7$ in figure 10. It is evident from this figure that vortex shedding at mid span leads in phase, while that near the cylinder free end or the wall lags significantly. The observation is fully consistent with the scenario that, under the downwash flow and boundary layer effects, the two ends of the spanwise vortex roll lean upstream towards the cylinder free end and the base, respectively. This observation is consistent with Tanaka and Murata's measurement (Tanaka & Murata 1999) in the wake of a wall-mounted

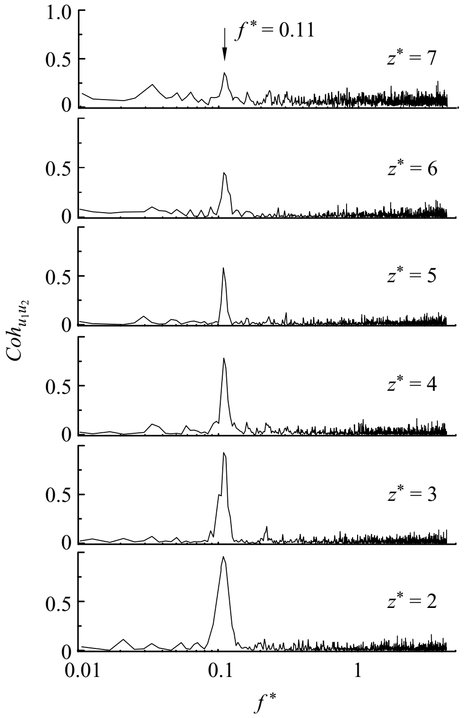

FIGURE 8. Spectral coherence $Coh_{u_1u_2}$ between streamwise fluctuating velocity u_1 and u_2 at $y^* = 2$, $H/d = 7$. u_1 was measured at $z^* = 1$ and u_2 was measured from $z^* = 2$–7.

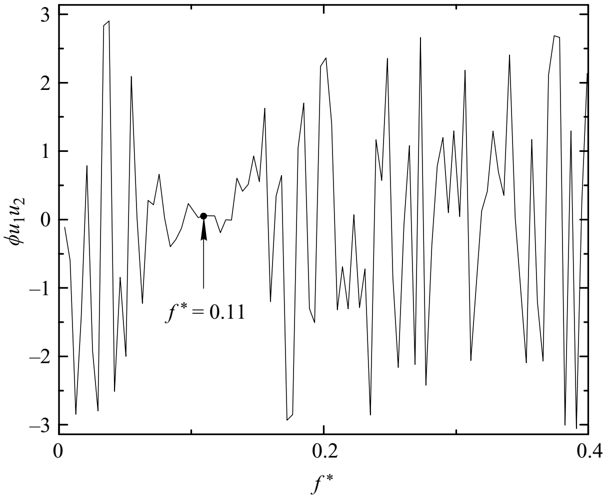

FIGURE 9. The phase shift between u_1 and u_2 at $x^* = 3$, $y^* = 2$, $H/d = 7$. u_1 was measured at $z^* = 1$ and u_2 was measured from $z^* = 2$.

finite-length circular cylinder ($H/d = 2.5 \sim 10$, $Re_d = 3.7 \times 10^4$). Their measured time-averaged vortex lines indicated that the spanwise vortex bends upstream near the free end and the wall, especially at a larger H/d.

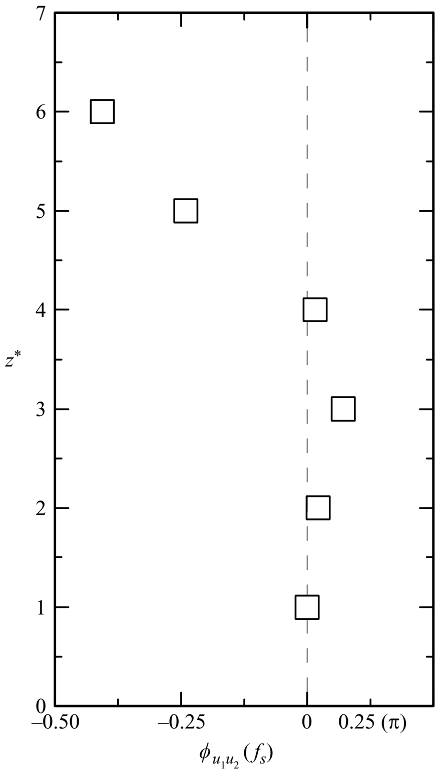

FIGURE 10. Dependence of the phase angle $\phi_{u_1u_2}(f_s)$ between streamwise fluctuating velocities u_1 and u_2 at $x^* = 3$ and $y^* = 2$ on spanwise location $z^*(H/d = 7)$, where u_1 was measured at $z^* = 1$ and u_2 was measured from $z^* = 2$–6.

4. Physical model of the near-wake organized structure

Experimental data unveils three types of vortical structures, i.e. the tip vortex emanating from the free end, Kármán vortices and the base vortex near the wall. What the interrelationship is among them has yet to be clarified. There is a general consensus that the downwash flow and the streamwise tip vortex are inherently connected. (e.g. Etzold & Fiedler 1976; Kawamura *et al.* 1984; Tanaka & Murata 1999; Park & Lee 2000; Sumner *et al.* 2004). Etzold & Fiedler (1976) and Kawamura *et al.* (1984) proposed the presence of a pair of conical steamwise vortices. In their proposed model (see figure 11 in Etzold & Fiedler 1976 and figure 19 in Kawamura *et al.* 1984), however, the spanwise vortex filaments near the free end were not closed. Based on time-averaged velocity measurements, Tanaka & Murata (1999) suggested that the time-averaged vortex lines from both sides of a wall-mounted finite-length circular cylinder were connected with each other near the free end, and the overall structure of the vortex lines appeared like an arch. Note that, if a vortex filament turns by 180°, the sense of rotation will be changed, that is, the connection of two counter-rotating vortex filaments is possible at their ends (Zdravkovich 2003). Based on flow visualization in the (x, y) planes at various spanwise locations $(H/d = 0.5 \sim 5, Re_d = 270 \sim 730)$, Sakamoto & Arie (1983) speculated that the flow separating from the free end connected the spanwise vortex separating from both sides of a finite-length cylinder, forming an arch-type structure. Under the effects of the free end downwash flow, the upper part of this arch-type vortex structure is bent upstream (figure 10), thus

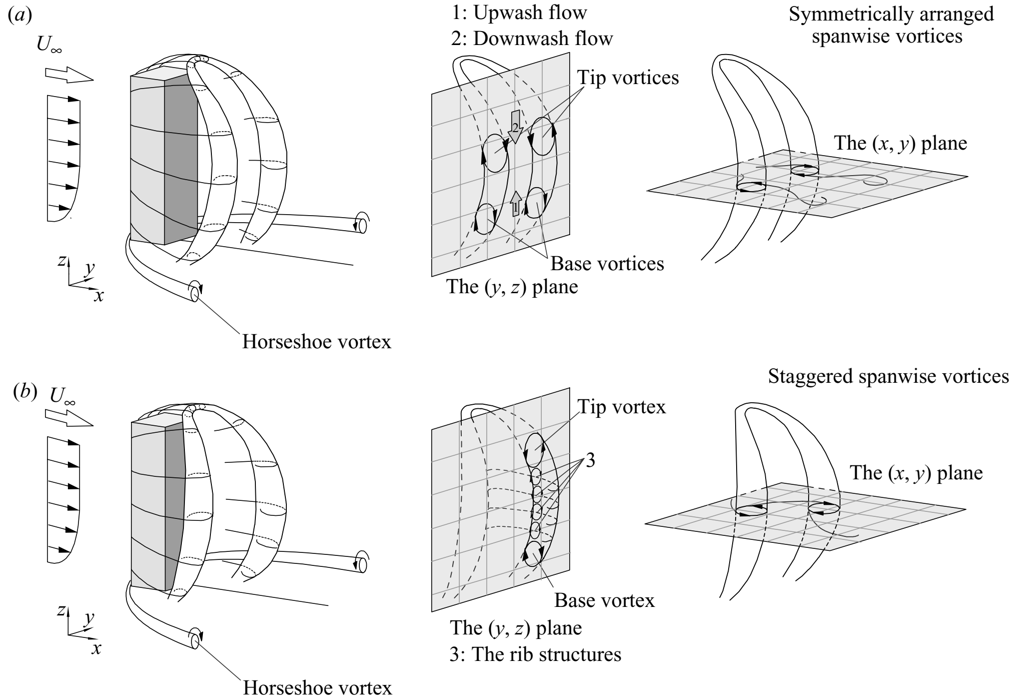

FIGURE 11. Model of the flow structure around a wall-mounted finite-length square cylinder: (*a*) symmetrically arranged two spanwise vortex roll, (*b*) staggered arranged spanwise vortex roll.

resulting in streamwise vortices in the (y, z) plane near the free end, i.e. the tip vortices (figure 6*c*,*d*).

The upwash flow and the base vortex were observed experimentally by Etzold & Fiedler (1976), Snyder & Lawson (1994), Summer *et al.* (2004) and Adaramola *et al.* (2006), but not by others (Kawamura *et al.* 1984; Okamoto & Sunabashiri 1992; Fröhlich & Rodi 2004; Afgan *et al.* 2007). One possible reason for the absence of upwash flow is the negligibly small effect of the boundary layer over the wall, where the finite-length cylinder was mounted. Wang *et al.* (2006) investigated the effects of the boundary layer on the near wake of a wall-mounted finite-length cylinder and concluded that, with increasing boundary layer thickness, the base vortex was enhanced, inducing a strong upwash flow from the wall. The upwash flow and the corresponding base vortex are presently evident in the (x, z) plane and (y, z) planes since the boundary layer has a thickness of around $1.35d$ (figure 3) and imposes a considerable effect.

Both Etzold & Fiedler (1976) and Sumner *et al.* (2004) attributed the base vortex to the oblique separation of Kármán vortex near the wall. With the wall approached, the convection velocity of spanwise vortices is reduced gradually under the influence of the boundary layer. Consequently, the spanwise vortex roll is inclined upstream near the wall. Similarly to the formation of tip vortices, the inclined spanwise vortex roll near the wall may be seen in the (y, z) plane as streamwise vortices, i.e. the base vortex, and may induce an upwash flow in the (x, z) plane (figure 4). However, there is a difference in the formation between the tip and base vortices. The spanwise shear layer, separating from the cylinder, near the wall will interact with the boundary layer.

As a matter of fact, very close to the wall the boundary layer effect may be so strong that the spanwise shear layer rollup might be overwhelmed, which is consistent with the view of Lighthill (1963) and Doligalski, Smith & Walker (1994).

Martinuzzi & Tropea (1993) observed the two tails of the horseshoe vortex encircling a wall-mounted cube based on their surface oil flow visualization. The horseshoe vortex formed at the junction of the obstacle front face and the wall, and tailed around the obstacle from both sides (Simpson 2001), whose imprint almost vanished at $z^* = 0.4$ for a wall-mounted circular cylinder (Sahin, Ozturk & Akilli 2007). This horseshoe vortex is however not observed presently (e.g. figure 6), which is ascribed to two reasons. First, the longitudinal vortical tails of the horseshoe vortex are very close to the wall (Simpson 2001), beyond the present measurement range of z^*. For instance, using a two-component LDA, Hussein & Martinuzzi (1996) measured the velocity distribution ($Re_d = 40\,000$) in a cross-stream plane downstream of a wall-mounted cube at $x^* = 0.75$, and identified the core of the horseshoe vortex tail only at $z^* \approx 0.15$. Second, the scale of the horseshoe vortex is very small, compared with spanwise or tip vortices. Lin, Ho & Dey (2008) estimated in the wake of a square cylinder with $H/d = 0.5 \sim 6.66$ that the scale of the horseshoe vortex was in the order of about $0.3d$. As such, it could not be resolved by the present PIV measurement with a spatial resolution of ~ 5 mm or $0.25d$ (§ 2.4). Nevertheless, the horseshoe vortex has been incorporated in the proposed flow model (figure 11) in view of the reports in the literature.

Based on the above results and discussion, a model is proposed for the flow structure behind a wall-mounted finite-length square cylinder, as sketched in figure 11. In this model, spanwise vortices from both sides of the cylinder are connected with each other near the free end, forming an arch-type vortex. This arch-type vortex structure consists of two 'legs' that immerse in the wall boundary layer and join each other near the cylinder free end. Under the influence of the free-end downwash flow and the boundary layer over the wall, both the upper and the lower parts of the arch-type structure are inclined upstream. This arch-type vortex is further accompanied by a horseshoe vortex which originates at the junction of the cylinder and the wall.

Two most representative instantaneous configurations of the arch-type vortex are illustrated in figure 11, corresponding to the two types of spanwise vortices discussed in § 3. Figure 11(*a*) presents one configuration of the flow structure with spanwise vortices symmetrically arranged, which conforms to the observation in figure 5(*d*–*f*). While joining each other near the free end, the two spanwise vortex rolls are inclined upstream, forming a pair of symmetrical tip vortices in the (y, z) plane. The tip vortices are inherently connected to downwash flow. Similarly, the spanwise vortices inclined upstream near the wall form another pair of streamwise vortices, i.e. the base vortices (figure 6*c*,*d*). The base vortices drive flow near $y^* = 0$ upwards from the wall, forming the upwash flow (figures 4*a* and 6*c*). It should be mentioned that the symmetrically arranged spanwise vortex rolls do not occur frequently, as will be discussed in § 5. Once spanwise vortices are symmetrically arranged, spanwise shear flow would not sweep across the central plane. Accordingly, the downwash and upwash flow is predominant in the (x, z) plane (figures 4*a* and 6*c*).

Figure 11(*b*) presents another typical configuration of instantaneous flow structure: two staggered spanwise vortex rolls. The corresponding spanwise vortices in the (x, y) plane are antisymmetrically arranged, as seen in figure 5(*a*–*c*). The longitudinal rib structures occur on one side of the cylinder in the (y, z) plane. So do the tip and base vortices, seen in the (y, z) plane (figure 6*a*,*b*).

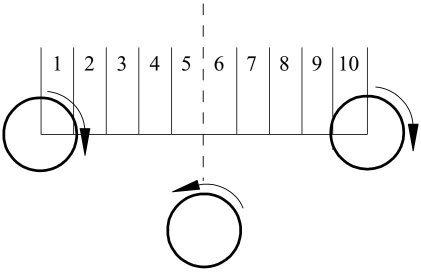

Region	Spatial configuration	Classification
1 or 10	1	Symmetric
2 or 9	2	Approximately symmetric
3 or 8	3	Neutral
4 or 7	4	Approximately anti symmetric
5 or 6	5	Anti symmetric

FIGURE 12. Classified spatial configurations of the two spanwise vortex rolls.

It should be pointed out based on the present data that the spanwise vortex rolls may not be perfectly symmetrically or antisymmetrically arranged. As a matter of fact, many of the spatial configurations of instantaneous spanwise vortices are something in between.

5. Discussion

5.1. *Spanwise dependence of vortex spatial configuration*

Insight into the near-wake physics may be gained by understanding statistically the spatial configuration of spanwise vortices in the (x, y) plane. To this end, we divide equally the centre-to-centre longitudinal spacing between two vortices of the same sign into ten regions, marked with 1–10 (figure 12). Five different configurations, i.e. symmetric, approximately symmetric, antisymmetric, approximately antisymmetric and neutral, may be classified based on which region an opposite-signed vortex centre falls in. The correspondence between the ten regions and the five configurations is shown in figure 12.

Figure 13 presents the probability density function (PDF), determined from 1500 instantaneous PIV images, for each of the five configurations at different spanwise locations ($H/d = 7$). Near the free end ($z^* = 6$), over 55 % (31 % + 24 %) spanwise vortices are symmetrical or approximately symmetrical, apparently linked to the free-end downwash flow that tends to alter antisymmetric to symmetric vortex shedding (Farivar 1981; Okamoto & Sunabashiri 1992; Wang *et al.* 2006). Okamoto & Sunabashiri (1992) examined vortex shedding along the span from a wall-mounted finite-length circular cylinder ($H/d = 7$, $Re_d = 1\,060$) and suggested that the antisymmetric vortices disappeared at 0.5d from the free end. However, the present data indicates the survival of about 13 % of antisymmetric vortices even at 1d away from the free end in the case of a square cylinder. The configurations of antisymmetrically and approximately antisymmetrical vortices account for 54 % (30 % + 24 %) at mid span ($z^* = 3.5$), exhibiting the dominance of alternate vortex shedding. Note that, even with a considerably larger H/d than $(H/d)_{cr} \approx 2$ proposed by Sakamoto & Arie (1983), more than 10 % of spanwise vortices are symmetrically

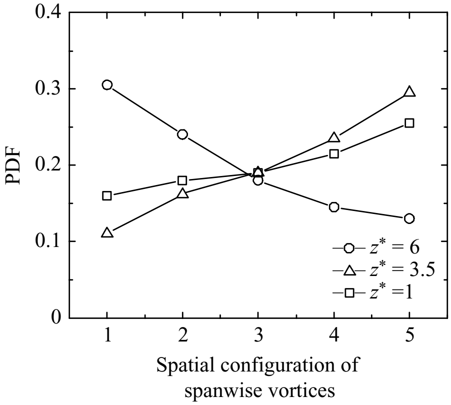

FIGURE 13. Probability density function of the occurrence of various spatial configurations of spanwise vortices ($H/d = 7$). Definitions for the spatial configuration are given in figure 12.

arranged. The PDF distribution at $z^* = 1$ is qualitatively similar to that at mid span, albeit with a smaller probability of antisymmetrical vortices and larger probability of symmetrical vortices, which suggests that the upwash flow near the wall also tends to enhance symmetrically arranged vortices (Wang *et al.* 2006).

Some remarks are due on the relationship between fluctuating lift (C'_L) and the spanwise vortex configuration. Given perfectly symmetric vortex shedding from a cylinder, C'_L is expected to be zero. Based on their strain-gauge measurements, Sakamoto & Oiwake (1984) reported $C'_L \approx 0.28 - 0.31$ for $H/d = 3 \sim 6$ ($Re_d = 2.97 \times 10^4$), which is substantially smaller than Vickery's measurement ($C'_L \approx 1.3$) in a two-dimensional square cylinder wake ($Re_d = 4 \times 10^4 - 1.5 \times 10^5$) (Vickery 1996). The decreased C'_L is attributed to the occurrence of symmetrically arranged vortices in a finite-length cylinder wake. A similar difference was also reported for the wall-mounted finite-length circular cylinder. Baban, So & Ötügen (1989) measured the sectional C'_L on a finite-length circular cylinder of $H/d = 3$, and found that C'_L decreased when approaching the cylinder free end, apparently owing to the increased probability of symmetrically arranged vortices (figure 13).

Figure 14 presents the spatial distribution of the vortex centres for symmetrically and antisymmetrically arranged vortices, along with the corresponding vortex trajectories. The vortex centres of the other three configurations (figure 12) occur generally between symmetrical and antisymmetrical vortex centres, thus not presented in figure 14 for clarity. The number of detected vortex centres reduces with x^* because of the increased breakup of spanwise vortices downstream. The trajectories were estimated from a least-square seventh-order polynomial fit to instantaneous vortex centre positions. The boundary of the time-averaged reverse flow zone is marked by a bold line, and the vortex trajectory behind a two-dimensional square cylinder (Lyn *et al.* 1995) is also given to provide a benchmark.

Except near the free end, the vortex trajectories in the finite-length cylinder wake occur further away from the centreline, compared with a two-dimensional cylinder wake (figure 14*e*,*f*), suggesting an increased wake width. The observation is probably ascribed to downwash and upwash flows, which entrain free-stream fluid into the wake and drive the spanwise vortices away from the centreline. At $z^* = 6$, the vortex centres of both symmetrical and antisymmetrical vortices occur in a limited downstream extent behind the cylinder, without any vortex detected beyond $x^* = 3.5$ (figure 14*a*)

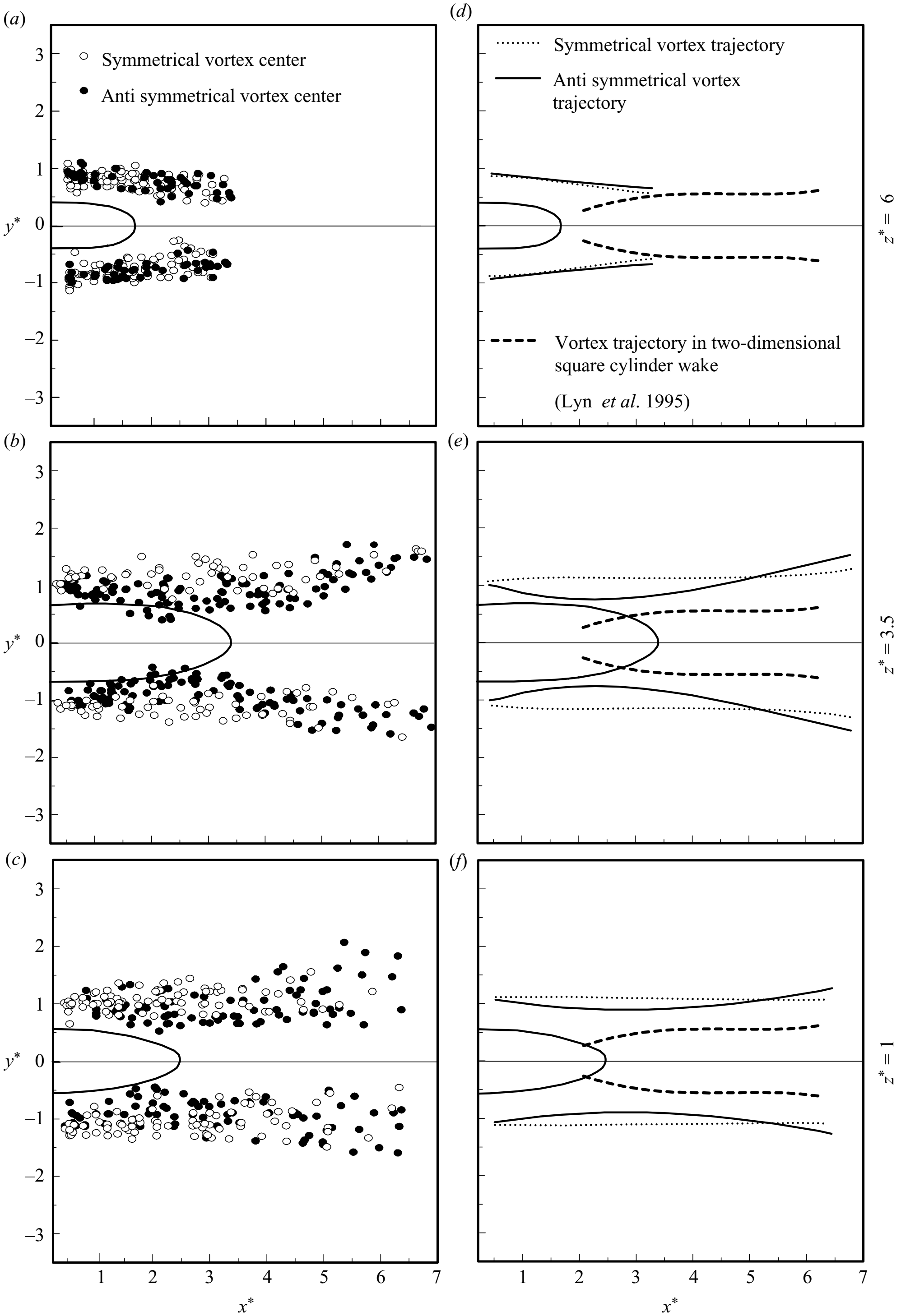

FIGURE 14. Distributions of detected vortex centres and corresponding vortex trajectory: (*a*, *d*) $z^* = 6$, (*b*, *e*) 3.5, (*c*, *f*) 1, $H/d = 7$. The bold line denotes the boundary of reverse flow zone, determined by $\overline{U^*} = 0$.

because the free-end downwash flow brings the separated vortices towards mid span, as supported later by flow visualization data. At $z^* = 3.5$, the trajectory of symmetrically arranged vortices is almost parallel to the centreline. The antisymmetrically arranged vortices occur nearer to the wake centreline initially, compared with the symmetrically arranged vortices, and then move apart downstream from $x^* \approx 2.5$ (figure 14*b*,*e*), which is qualitatively similar to vortex trajectories behind a two-dimensional square cylinder. The distribution of the vortex centres at $z^* = 1$ (figure 14*c*,*f*) is essentially similar to that at mid span. Nevertheless, the difference between the trajectories of symmetrically and antisymmetrically arranged vortices is less pronounced, probably owing to the strong influence of the wall.

In view of the difference in the formation mechanism of antisymmetrically and symmetrically arranged spanwise vortices, it could be insightful to examine and compare the flow fields associated with the two distinct configurations. To this end, the ensemble averages were taken from images of the symmetrical configuration (a total of 453 at $z^* = 6$ and 156 at $z^* = 3.5$) and antisymmetrical configuration (a total of 196 at $z^* = 6$ and 448 at $z^* = 3.5$). Figures 15 and 16 compare the ensemble-averaged streamwise velocity $<U^*>$ and the velocity products $<u^{2*}>$, $<v^{2*}>$ and $<u^*v^*>$ of the second order between the two configurations at $z^* = 6$ and 3.5, respectively. The time-averaged results, i.e. $\overline{U^*}$, $\overline{u^{2*}}$, $\overline{v^{2*}}$ and $\overline{u^*v^*}$ from 1500 PIV-measured instantaneous images are also included in the figures. The results at $z^* = 1$ are quite similar to those at $z^* = 3.5$ (figure 16) and are therefore not presented.

Near the free end ($z^* = 6$), all the contours appear to converge towards the centreline with increasing x^* due to downwash flow from the free end. The $<U^*>$ contours, irrespective of the symmetrical or antisymmetrical configuration, resemble those of $\overline{U^*}$ (figure 15*a*–*c*), except that the streamwise extent of the reverse flow zone ($<U^*> = 0$) is slightly smaller for the symmetrical configuration (figure 15*c*) than for the antisymmetrical (figure 15*b*). The result is consistent with the conception that the symmetrically arranged vortices tend to be associated with a predominant downwash flow, which acts to suppress alternate spanwise vortex shedding, thus reducing the reverse flow zone (Wang *et al.* 2006). The contours of $\overline{u^{2*}}$ (figure 15*d*) and $<u^{2*}>$ (figure 15*e*) of the antisymmetrical configuration display two peaks, with the maximum occurring at about the same position, i.e. $(x^*, y^*) \approx (2.0, \pm 0.6)$. In contrast, one peak only is seen in the $<u^{2*}>$ contours of the symmetrical configuration (figure 15*f*) and the peak value (0.025) is appreciably smaller than its counterpart (0.029) in figure 15(*e*). The difference in the maximum contour level is even more significant in $<v^{2*}>$; the maximum $<v^{2*}>$ is 0.0045 for symmetrical configuration (figure 15*i*) but 0.0093 for the antisymmetrical (figure 15*h*). The observation is consistent with previous reports (Sakamoto & Arie 1983; Bisset, Antonia & Browne 1990; Zhou & Antonia 1993) that the velocity fluctuation associated with antisymmetrically arranged vortices was greater than that with symmetrical vortices since the former tended to reinforce each other, especially in the lateral motion, thus resulting in larger $<u^{2*}>$ and $<v^{2*}>$ than the symmetrically arranged. For the same reason, the maximum magnitude of $<u^*v^*>$ of the antisymmetrical configuration (figure 15*k*) is larger than that of the symmetrical configuration (figure 15*l*).

At mid span ($z^* = 3.5$), the contours diverge with increasing x^*, consistent with the downstream growth in the wake width. The difference between the antisymmetrical and symmetrical configurations is more pronounced. The streamwise extent of the reverse flow zone in the antisymmetrical configuration (figure 16*b*) reaches $x^* = 2.2$, around half of that in the symmetrical (figure 16*c*). In a two-dimensional square cylinder wake ($Re_d = 21\,400$), the reverse flow zone is even shorter, $x^* \approx 0.92$ (Lyn

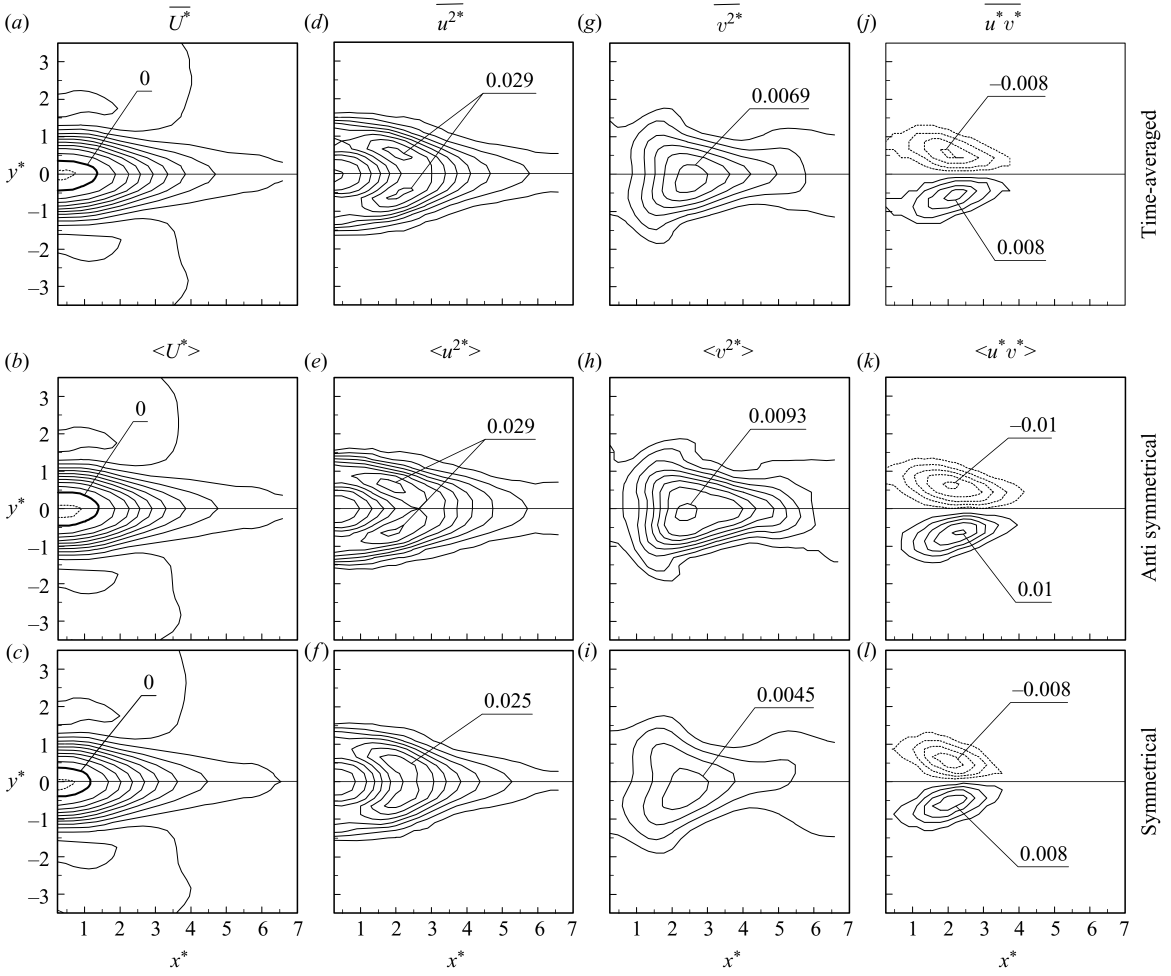

FIGURE 15. Time-averaged contours: $\overline{U^*}$, $\overline{u^{2*}}$, $\overline{v^{2*}}$, $\overline{u^*v^*}$ (*a*, *d*, *g*, *j*). Ensemble-averaged contours: $<U^*>$, $<u^{2*}>$, $<v^{2*}>$ and $<u^*v^*>$ for antisymmetrical (*b*, *e*, *h*, *k*) and symmetrical configuration (*c*, *f*, *i*, *l*). (*a–c*) Contour interval = 0.1; (*d–f*) 0.004; (*g–i*) 0.0012 and (*j–l*) 0.002. $z^* = 6$.

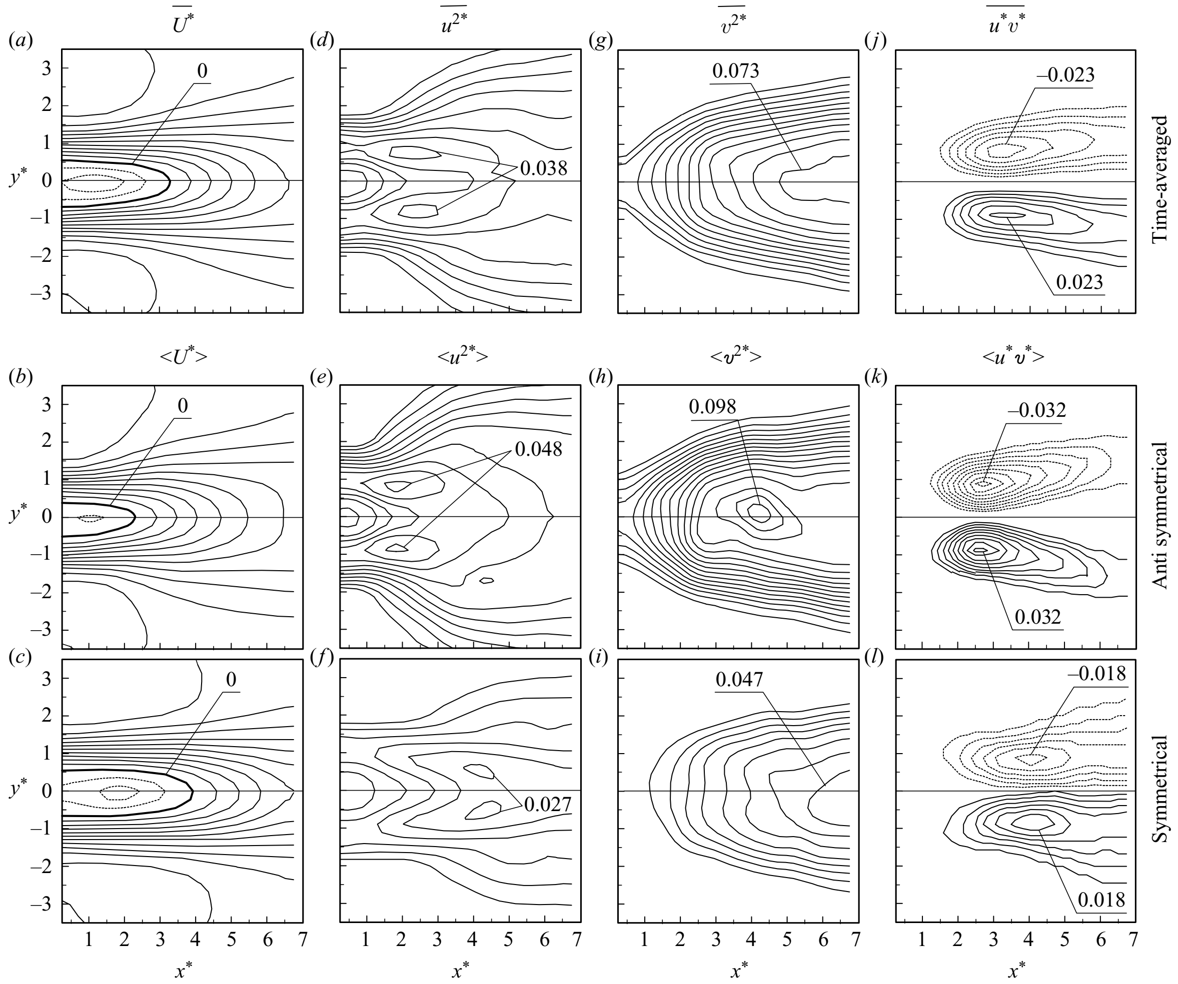

FIGURE 16. Time-averaged contours: $\overline{U^*}$, $\overline{u^{2*}}$, $\overline{v^{2*}}$, $\overline{u^*v^*}$ (*a*, *d*, *g*, *j*). Ensemble-averaged contours: $<U^*>$, $<u^{2*}>$, $<v^{2*}>$ and $<u^*v^*>$ for antisymmetrical (*b*, *e*, *h*, *k*) and symmetrical configuration (*c*, *f*, *i*, *l*). (*a*–*c*) Contour interval = 0.1; (*d*–*f*) 0.004; (*g*–*i*) 0.0052 and (*j*–*l*) 0.0064. $z^* = 3.5$.

et al. 1995). A shorter reversed flow zone implies stronger entrainment of high-speed free-stream fluid into the wake, i.e. stronger vortex shedding (Wang *et al.* 2006). The difference between the antisymmetrical and symmetrical configurations is contrary to that near the free end ($z^* = 6$), where the reverse flow zone is shorter in the symmetrical configuration owing to the strong influence of downwash flow, not necessarily related to the strength of vortex shedding. Noting that the contour increment is identical in figure 16(*a–c*), the $<U^*>$ contours along the centreline are more densely distributed in the antisymmetrical configuration (figure 16*b*) than in the symmetrical (figure 16*c*), indicating a faster recovery of velocity deficit, i.e. stronger vortex shedding and entrainment of free-stream fluid into the wake. The maximum $<u^{2*}>$, $<v^{2*}>$ and $<u^* v^*>$ are 0.048, 0.098 and 0.032, respectively, in the antisymmetrical configuration, considerably higher than their counterparts, 0.027, 0.047 and 0.018, in the symmetrical, which is internally consistent with the observation from the $<U^*>$ contours.

Following Bloor (1964), the location where the streamwise fluctuating velocity reaches its maximum may be used to estimate the vortex formation length. This length is closely connected to the drag. A short length corresponds to a large drag or vice versa (Bloor 1964; Balachandar, Mittal & Najjar 1997; Zdravkovich 1997). The maximum $\overline{u^{2*}}$ (figure 16*d*) occurs at $x^* \approx 2.3$, significantly larger than that (1.5) in a two-dimensional square cylinder wake (Lyn *et al.* 1995; Saha, Muralidhar & Biswas 2000). The observation conforms to previous reports that the time-averaged drag coefficient C_D in a finite-length cylinder wake is significantly smaller than in a two-dimensional cylinder wake (e.g. Okamoto & Yagita 1973; Farivar 1981; Sarode *et al.* 1981; Okamoto & Sunabashiri 1992). The formation length of the antisymmetrical vortices is 1.9, only slightly bigger than its two-dimensional counterpart but much smaller than that (4.2) of the symmetrical (figure 16*e*). Evidently, the drag associated with the symmetrically arranged vortices is much smaller than that with the antisymmetrical, accounting largely for the reduced C_D in a finite-length cylinder wake.

The difference in $\overline{v^{2*}}$ and $<v^{2*}>$ (or $\overline{u^* v^*}$ and $<u^* v^*>$) between the configurations (figure 16g-*l*) is qualitatively similar to that near the free end (figure 15).

5.2. *Interconnected vortical structures*

The near wake of a finite-length cylinder is dominated by three types of vortical structures (spanwise, tip and base vortices) and their interactions. Insight into the interrelationship between the three types of vortices may be gained by examining flow visualization photographs ($Re_d = 221$) captured simultaneously in the (x, y) plane at $z^* = 6$ and the (x, z) plane at $y^* = 0$. Figure 17(*a*) displays a number of symmetrically arranged vortical structures, consistent with the occurrence of the Kelvin–Helmholtz (K-H) vortices in the separating shear layer. Figure 17(*b*) shows the rollup and descent of the free-end shear layer. The descending free-end shear layer leads to the disappearance of vortical structures in the (x, y) plane ($z^* = 6$) downstream from the fourth vortex marked in figure 17(*a*). As marked by 1, 2, 3 and 4, there is an excellent correspondence between the rollup structures in the (x, y) plane and the (x, z) plane (figure 17). This correspondence indicates unequivocally a physical connection between the flow structures in the two planes, that is, each pair of symmetric vortices seen in the (x, y) plane and the corresponding rollup structure separating from the free end are part of the same vortical structure, as depicted in the proposed flow structure model in figure 11.

Okamoto & Sunabashiri (1992) examined spanwise vortices ($Re_d \approx 1\,000$) at different spanwise locations and suggested that the symmetric vortices occur near the free end, while the antisymmetric vortices occur sufficiently far away from the free

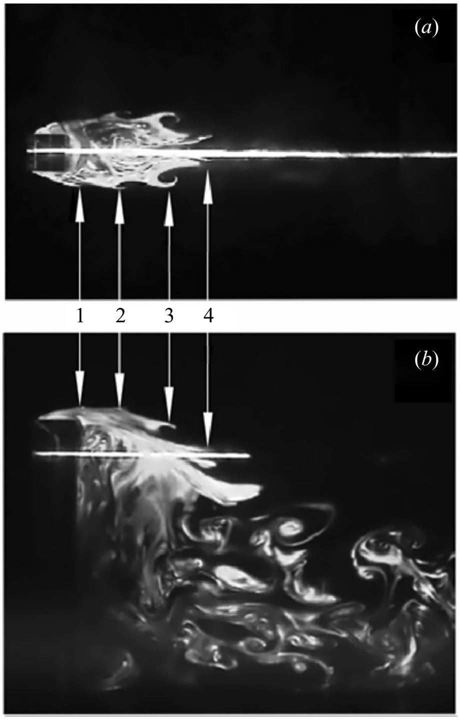

FIGURE 17. Flow visualization images ($H/d = 7$) simultaneously captured in (*a*) the (x, y) plane at $z^* = 6$ and (*b*) the (x, z) plane at $y^* = 0$.

end. The present flow visualization photograph at $Re_d = 221$ shows only the symmetric spanwise vortices at $z^* = 6$ (figure 17*a*), no antisymmetric vortices at all. This is in distinct contrast with the PIV results (figure 5*a*,*d*), where both configurations of vortices may occur near the free end at $Re_d = 9\,300$. The occurrence of antisymmetric vortices near the free end is apparently due to turbulence at the higher Reynolds number, which is associated with instability and hence unsteady flow separation.

Flow visualization was also conducted at $z^* = 3.5$ and 1. Both antisymmetrical and symmetrical spanwise vortices (figures 18*a*,*b* and 19*a*,*b*) occur, consistent with PIV measurements at $Re_d = 9300$ (figure 4*b*, *c*, *e*, *f*). Note that, the formation of typical antisymmetrical Kármán vortices shown in figures 18(*a*) and 19(*a*) is rather different from that behind a two-dimensional cylinder. For example, the former is less organized than the latter. The relatively small-scale K-H vortices in the shear layers separating from the cylinder are marked with 1–3, the subscripts '*p*' and '*n*' indicating positive- and negative-signed vortices, respectively. It appears that the K-H vortices are initially formed symmetrically, e.g. 1_n and 1_p, 2_n and 2_p in figure 18(*b*) and 1_n and 1_p in figure 19(*a*), though turning into staggered Kármán vortices later because of the inherent instability of the symmetric arrangement.

5.3. *Effect of the height-to-width ratio on the flow structure*

5.3.1. *Flow field in the (x, z) plane*

As H/d reduces to 5 and 3, typical instantaneous and time-averaged streamlines in the (x, z) plane at $y^* = 0$ (not shown) are topologically similar to those at $H/d = 7$ (figure 4), that is, the flow structure is qualitatively unchanged. However, there is a

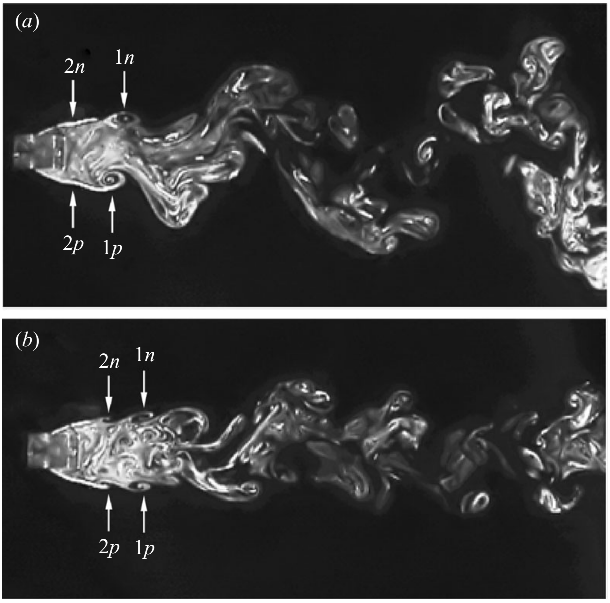

FIGURE 18. Spanwise flow structures in the (x, y) plane at $z^* = 3.5$, $H/d = 7$: (*a*) antisymmetrical Kármán vortices, (*b*) symmetrical vortices. The numbers indicate the order of small-scale positive (*p*) or negative (*n*) K-H vortices.

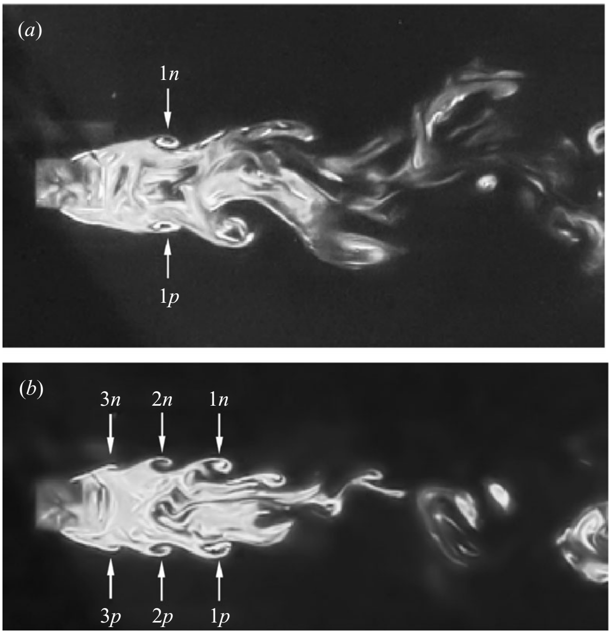

FIGURE 19. Spanwise flow structures in the (x, y) plane at $z^* = 1$, $H/d = 7$: (*a*) antisymmetrical Kármán vortices, (*b*) symmetrical vortices. The numbers indicate the order of small-scale positive (*p*) or negative (*n*) K-H vortices.

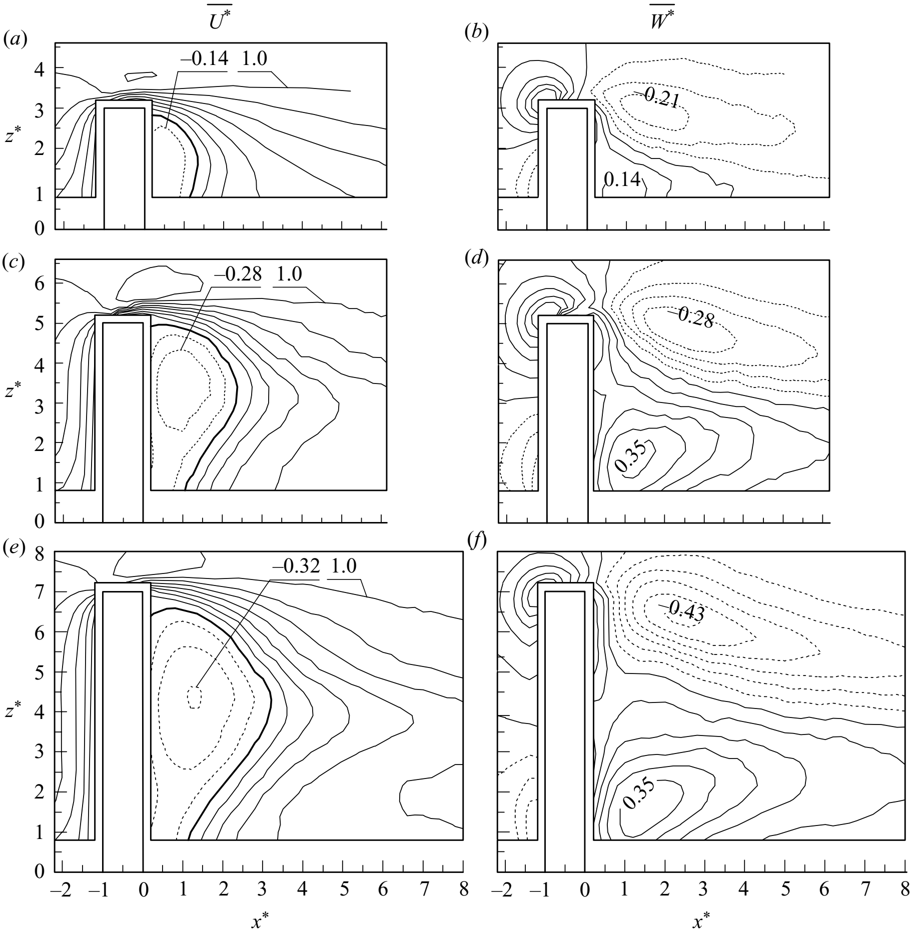

FIGURE 20. Time-averaged counters of $\overline{U^*}$ and $\overline{W^*}$in the (x, z) plane ($y^* = 0$). (*a*) The minimum level, −0.14; the maximum level, 1.14, contour interval = 0.14; (*b*) −0.21, 0.28, 0.07; (*c*) −0.28, 1.14, 0.14; (*d*) −0.28, 0.36, 0.07; (*e*) −0.43, 1.14, 0.14; (*f*) −0.43, 0.36, 0.07. The bold line denotes the boundary of reverse flow zone, determined by $\overline{U^*} = 0$. (*a*, *b*) $H/d = 3$, (*c*, *d*) 5 and (*e*, *f*) 7.

discernible difference with varying H/d. First, the recirculation region near the free end diminishes appreciably in size for smaller H/d, suggesting weakened downwash flow and probably also weakened upwash flow. As a result, the downstream extent of the averaged downwash or upwash flow region, which is marked by the saddle point in the averaged streamlines (figure 4*c*), shrinks for smaller H/d. Second, the counter-rotating foci in figure 4(*b*) could not be observed because of impaired spanwise vortex shedding with decreasing H/d.

Figures 20 and 21 present the contours of LDV-measured time-averaged streamwise and spanwise velocities and Reynolds stresses, i.e. $\overline{U^*}$, $\overline{W^*}$, $\overline{u^{2*}}$, $\overline{w^{2*}}$, $\overline{u^*w^*}$, in the (x, z) plane at $y^* = 0$. A number of observations can be made:

First, $\overline{U^*}$ (figure 20*a*,*c*,*e*) depends strongly on H/d. With H/d increasing from 3 to 7, the reverse flow zone is enlarged significantly and the maximum reverse flow velocity increases from −0.14 to −0.32.

Second, both upwash and downwash flows, best viewed from the contours of $\overline{W^*}$, exhibit a strong dependence on H/d, as shown in figure 20(*b*, *d*, *f*). The maximum

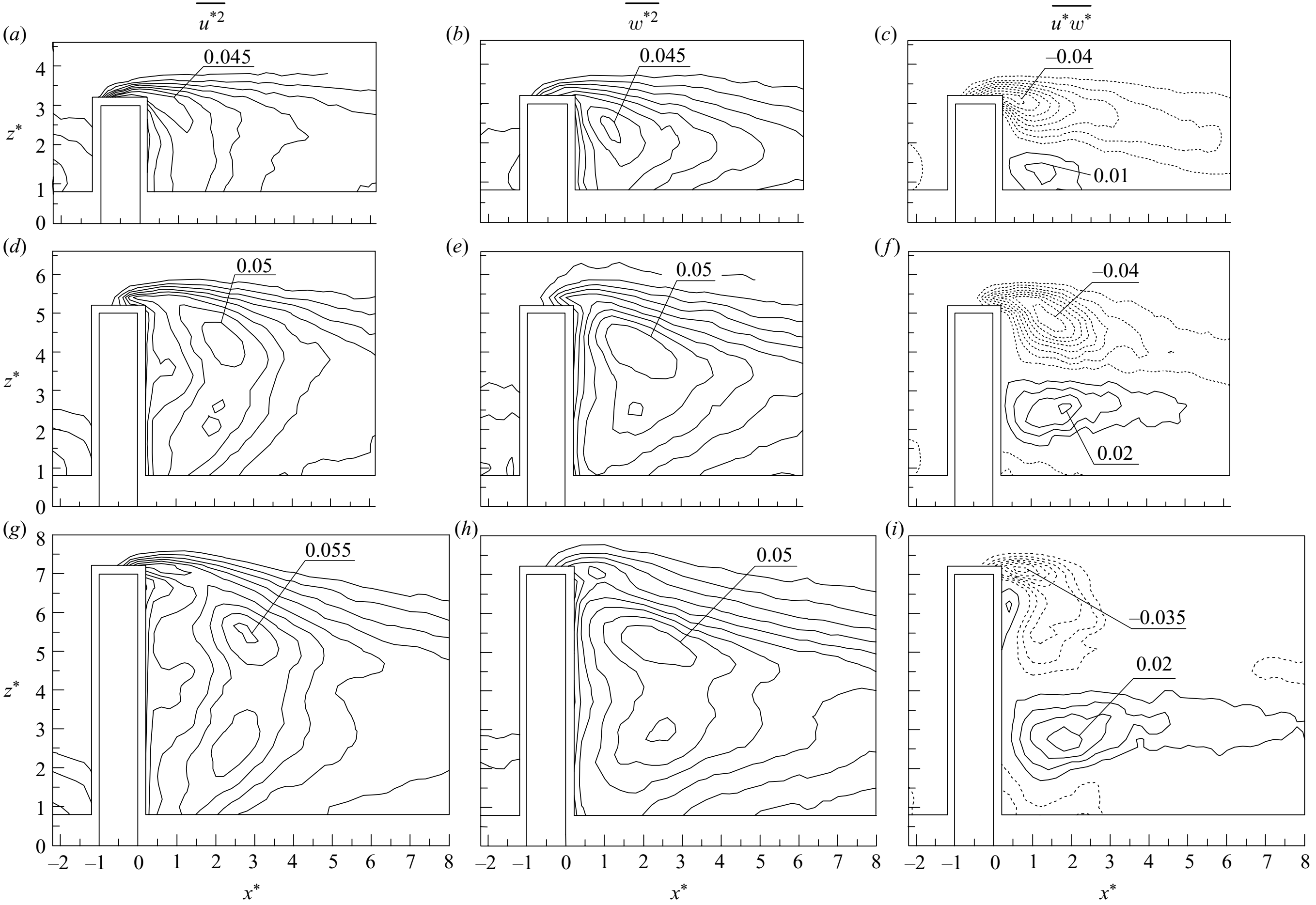

FIGURE 21. Contours of time-averaged Reynolds stresses in the (x, z) plane $(y^* = 0)$: (*a*) contour interval = 0.005, (*b*) 0.005, (*c*) 0.005, (*d*) 0.005, (*e*) 0.005, (*f*) 0.005, (*g*) 0.005, (*h*) 0.005, (*i*) 0.005. (*a*, *b*, *c*) $H/d = 3$, (*d*, *e*, *f*) 5 and (*g*, *h*, *i*) 7.

downwash velocity magnitude is doubled, from -0.21 at $H/d = 3$ to -0.43 at $H/d = 7$. The maximum upwash flow velocity grows from 0.14 at $H/d = 3$ to 0.35 at $H/d = 5$ and remains unchanged up to $H/d = 7$; nevertheless, the size of the same level contours increases progressively from $H/d = 3$ to 7. The observation indicates that both downwash and upwash flows are enhanced with increasing H/d, similarly to that observed in a finite-length circular cylinder wake ($H/d = 3 \sim 9$, Sumner *et al.* 2004). Based on their time-averaged measurements behind a wall-mounted finite-length circular cylinder in the (y, z) planes at $x^* = 4 \sim 10$, Sumner *et al.* (2004) inferred the presence of both the downwash and upwash flows at $H/d = 5 \sim 9$ but the absence of the upwash flow at $H/d = 3$. Their measurements for $H/d = 3$ were performed only at $x^* = 6$, where the upwash flow, decaying rapidly downstream (Wang *et al.* 2006), may have vanished, as confirmed by the streamlines at $H/d = 3$, which are parallel at $x^* \geqslant 5$. However, the upwash flow (positive $\overline{W^*}$) is evident for $x^* < 4$ in figure 20(b), conforming to Synder and Lawson's report (Synder & Lawson 1994) in the wake of a finite-length square cylinder ($H/d = 3$).

Third, the maximum magnitude in $\overline{W^*}$ associated with downwash flow occurs further downstream than that with upwash flow for all H/d, and the upwash flow decays more rapidly downstream than the downwash, especially at a small H/d.

Fourth, the maximum $\overline{u^{2*}}$and $\overline{w^{2*}}$ in the upper half of the wake increase slightly and progressively from $H/d = 3$ to 7, probably attributed to the enhanced spanwise vortices and tip vortices with increasing H/d. Note that both $\overline{u^{2*}}$and $\overline{w^{2*}}$ contours display two spanwise separated concentrations at $H/d = 7$ and also 5 (figure 21d,e,g,h), resulting from the three dimensionality of tip and base vortices, as supported by their absence further downstream. There is no such concentration in the lower half of the wake at $H/d = 3$ (figure 21a,b) owing to the weakening base vortices at small H/d.

Finally, the downwash and upwash flows have a pronounced effect on $\overline{u^* w^*}$ or spanwise momentum transport and this effect also depends on H/d. In general, $\overline{u^* w^*}$ (figure 21c, f, i) is negative in the upper part of the wake because the downwash flow ($w < 0$) is associated with the high-momentum fluid ($u > 0$) entrained from the free stream. On the other hand, $\overline{u^* w^*}$ is positive in the lower part of the wake because the upwash flow ($w > 0$) is also associated with high momentum fluid ($u > 0$) entrained from the potential flow. While the positive-valued contours expand gradually from $H/d = 3$ to 7 due to the enhanced upwash flow, the negative-valued contours shrink significantly. Note that $\overline{u^* w^*}$ is negative about the cylinder base for $H/d = 5$ and 7 because the strong upwash flow ($w > 0$) in this H/d range may bring up low-momentum flow ($u < 0$) from the boundary layer. On the other hand, the upwash flow at $H/d = 3$, though bringing up the low-momentum fluid from the boundary layer, may be too weak to produce any appreciable effect on $\overline{u^* w^*}$.

The reverse flow zone depends on H/d. In order to understand this dependence thoroughly, supplementary experiments were conducted at $H/d = 9$ and 11. The results, along with those reported in the literature, are summarized in figure 22. Lyn *et al.*'s data obtained in a two-dimensional square cylinder wake is also included (Lyn *et al.* 1995).

In a two-dimensional cylinder wake, the longitudinal length of the reverse flow zone is closely related to C_D and C_L'; in general, a short length corresponds to large C_D and C_L' (Bloor 1964; Zdravkovich 1997). This relation is however not applicable for the highly three-dimensional wake of a wall-mounted finite-length cylinder (to be explained later). The longitudinal length (figure 22a) of the reverse flow zone in a finite-length cylinder wake exceeds considerably the two-dimensional case, irrespective of H/d. The maximum length (L^*_{max}) occurs at the position of the saddle point shown

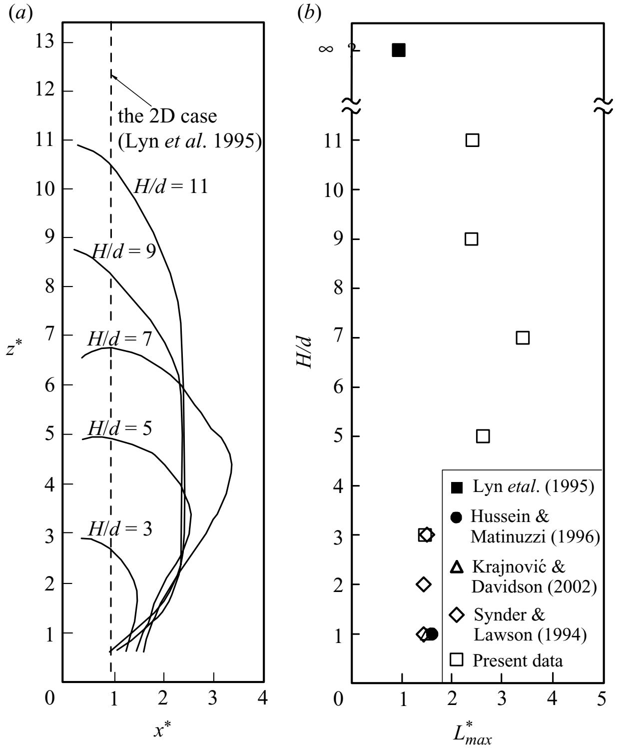

FIGURE 22. Dependence on H/d of (a) the time-averaged reverse flow zone and (b) the maximum longitudinal length of this zone.

in figure 4(c). There is no plateau in the reverse flow zone around this point for $H/d \leqslant 7$. Beyond $H/d = 7$, a plateau occurs along the cylinder span over the middle part and L^*_{max} changes very slowly. The observation is essentially consistent with the reports of Etzold & Fiedler (1976) and Okamoto & Sunabishiri (1992). The streamwise extent of the reverse flow zone reduces with the cylinder free end and wall approached owing to the effects of upwash and downwash flows (Wang *et al.* 2006).

The dependence of L^*_{max} on H/d (figure 22b) may be determined based on the present data, along with those in the literature. L^*_{max} is about 1.4, with little variation, from $H/d = 1$ to 3, where spanwise vortex shedding is largely subdued (Sakamoto & Arie 1983). However, it is stretched rapidly from 1.4 to 3.4 with H/d increasing from 3 to 7, and then contracts to 2.5 as H/d increases to 9. Beyond $H/d = 9$, it retreats very slowly until reaching a minimum of approximately 0.9 as $H/d \rightarrow \infty$ (Lyn *et al.* 1995). The result resembles that in a finite-length circular cylinder wake (Etzold & Fiedler 1976), where the maximum longitudinal length of the reverse flow zone occurs at $H/d \approx 6.5$.

The dependence of C_D and C'_L on H/d has been previously investigated. For example, Sarode *et al.* (1981), Kawamura *et al.* (1984) and Okamoto & Yagita (1973) measured C_D on a finite-length circular cylinder by integrating the surface pressure distribution; Sakamoto & Oiwake (1984) and Sumner *et al.* (2004) measured C_D and C'_L on a finite-length cylinder with a strain-gauge balance or load cell. The investigations documented a monotonically decreasing C_D or C'_L with decreasing H/d. Apparently, the occurrence of the maximum L^*_{max} (presently at $H/d = 7$) does

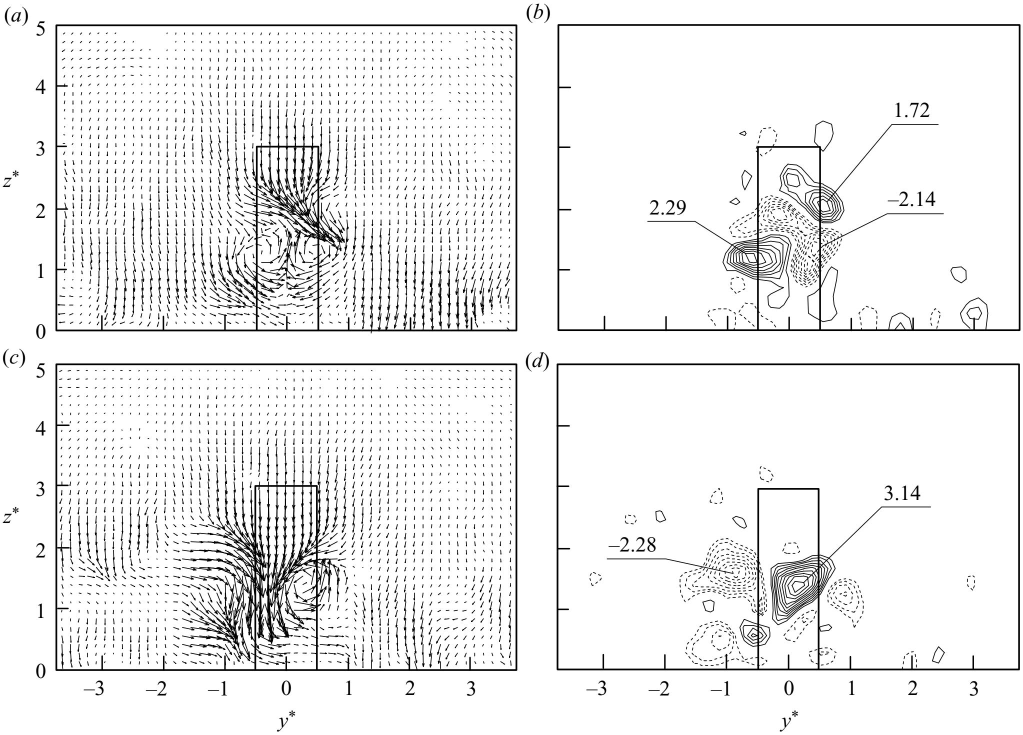

FIGURE 23. Instantaneous velocity vectors (*a*, *c*) and the corresponding ω_x^* contours (*b*, *d*) in the (*y*, *z*) plane at $x^* = 3$, $H/d = 3$. The ω_x^* contour interval is 0.286.

not necessarily corresponds to the smallest C_D or C_L'. The monotonic decrease in C_D and C_L' with reducing H/d is largely attributed to two reasons. First, spanwise vortex shedding impairs gradually (Okamoto & Sunabashiri 1992). Second, the probability of symmetrically arranged spanwise vortices grows, overwhelming the antisymmetrically arranged ones at a small H/d (Skamoto & Arie 1983).

5.3.2. *Flow field in the (y, z) plane*

The two typical instantaneous flow structures in the (*y*, *z*) plane observed at $H/d = 7$ (figure 6) are also seen at $H/d = 5$ and 3 (not shown). It has been noted that, in the absence of spanwise vortex shedding, both tip and base vortices may occur in pair simultaneously at $H/d = 7$ and 5 (e.g. figure 6*c*,*d*). However, only one pair of vortices occurs at $H/d = 3$, that is, the tip and the base vortices are not seen simultaneously. Figure 23 (*a*, *b*) illustrates the occurrence of one pair of predominant base vortices, which are associated with the upwash flow. On the other hand, the symmetrical occurrence of one pair of tip vortices, associated with downwash flow, is also observed with base vortices absent, as illustrated in figure 23(*c*,*d*). This is not unexpected since the interaction between the free-end downwash flow and upwash flow intensifies at very small H/d. As a matter of fact, at $H/d = 1$, the time-averaged free-end downwash flow reattached the wall and completely suppressed upwash flow and the formation of base vortices (Hussein & Martinuzzi 1996; Krajnović & Davidson 2002).

The downstream evolution of both tip and base vortices and its dependence on H/d may be examined through the contours of time-averaged streamwise vorticity ($\overline{\omega_x^*}$) at $x^* = 1$, 3 and 5 for $H/d = 3$, 5 and 7 (figure 24), which conform to our proposed

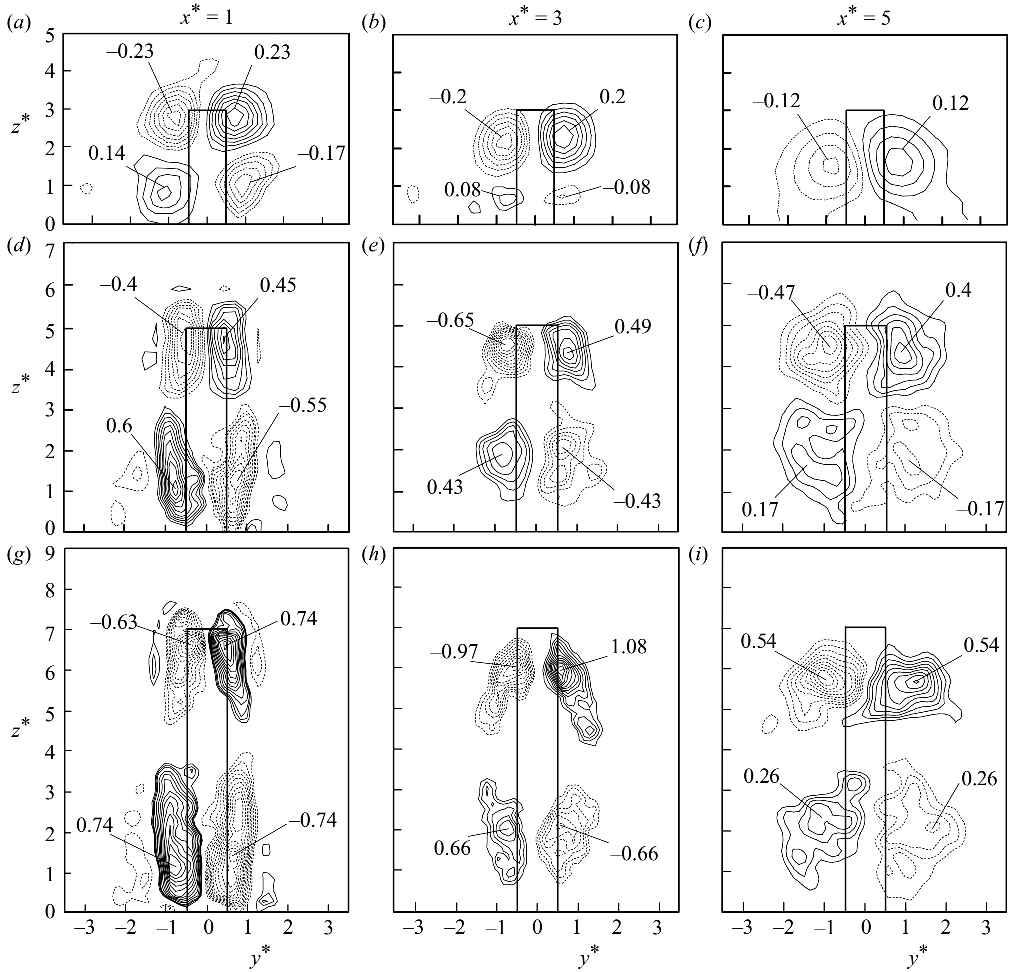

FIGURE 24. Contours of time-averaged streamwise vorticity $\overline{\omega_x^*}$: (a–c) $H/d=3$, (d–f) 5, (g–i) 7. (a) contour interval = 0.03, (b) 0.03, (c) 0.03, (d) 0.057, (e) 0.03, (f) 0.07, (g) 0.057, (h) 0.07, (i) 0.07.

model (figure 11). At $x^*=1$, the $\overline{\omega_x^*}$ contours are qualitatively similar for all H/d, displaying one pair of counter-rotating tip vortices near the free end and another pair of base vortices near the wall, with the opposite sense of rotation to the tip vortices. Furthermore, the strength of the vortices grows with increasing H/d. The longitudinal ‘mushroom’ structures observed in the instantaneous results at $H/d=5$ and 7 (e.g. figure 6a,b) occur rather randomly on either side of the cylinder, thus being averaged out and disappearing in the $\overline{\omega_x^*}$ contours (figure 24).

At $H/d=3$, both tip and base vortices decay in the maximum $\overline{\omega_x^*}$ with increasing x^*. The base vortices exhibit a much more rapid decay, only discernible at $x^*=3$ and completely disappearing at $x^*=5$, which is internally consistent with the absence of upwash flow at $x^*\geqslant 5$ as shown in figure 20(b). At $H/d=5$ and 7, the base vortex again decays downstream monotonically, though less rapidly than at $H/d=3$. The downstream evolution of the $\overline{\omega_x^*}$ contours correlates well with that of the $\overline{W^*}$ contours in the $(x,\, z)$ plane (figure 20b, d, f). The upwash flow is seen to weaken more quickly downstream than the downwash. Accordingly, the base vortex decays earlier than the tip vortex (figure 24). The maximum upwash flow velocity occurs at $x^* \approx 1.0 - 1.5$ for $H/d = 3$, 5 and 7. Subsequently, the base vortex is strongest at $x^* = 1$. The maximum downwash flow occurs at $x^* \approx 2.5$ for $H/d = 5$ and 7; the tip vortex strength reaches its maximum at $x^* = 3$ (figure 24*e*,*h*). The observation is consistent with the inherent association of the tip and base vortices with downwash and upwash flows, respectively.

6. Conclusions

Flow around a wall-mounted finite-length square cylinder has been systematically investigated. The cylinder is partially immersed in a boundary layer of $\delta/d = 1.35$. The H/d range examined was from 3 to 11. PIV measurements were conducted in the (x, z) plane at $y^* = 0$, and three (x, y) planes along the cylinder span and three (y, z) planes over $x^* = 1 \sim 5$, along with LDA and hotwire measurements. The following conclusions may be drawn from the analysis of the data:

(*a*) Flow around a finite-length square cylinder is highly three-dimensional, consisting of free-end downwash flow, spanwise shear flow and upwash flow from the wall. The near wake is characterized by the interactions between the three components. A physical model is proposed for the flow structure, as sketched in figure 11, which is distinct from previously proposed models. Both tip and base vortices are inherently connected with the spanwise vortex; the three types of vortices are all part of the same entity, viz. an arch-type organized structure, regardless of H/d. Under the effect of the free-end downwash flow, the upper part of the arch-type structure bends upstream, resulting in a pair of streamwise vortices near the free end, i.e. the tip vortices; the lower part also leans upstream near the wall because of the deficit of the convection velocity within the boundary layer, thus forming another pair of streamwise vortices, i.e. the base vortex. Both tip and base vortices are inherently associated with the free-end downwash and upwash flows, respectively.

(*b*) The spatial configuration of the two opposite-signed vortex rolls is much more complicated than in a two-dimensional wake, and depends on the interaction between Kármán vortex shedding and the downwash/upwash flows. Whilst the former is inherently antisymmetric, the latter promotes symmetric vortex shedding. Both antisymmetrical and symmetrical configurations have been observed throughout cylinder span. The two types of vortices follow rather distinct trajectories, which are farther from the centreline than those in a two-dimensional wake. The probability of antisymmetrically arranged vortices is largest at mid span and reduces significantly with the cylinder free end or the wall approached. The antisymmetrical vortices are associated with larger Reynolds stresses than the symmetrical. As such, the spanwise variation of Reynolds stresses in the near wake correlates well with the probabilities of the vortex configurations, that is, the stresses are strongest about the mid span and weakened with cylinder ends approached. Since symmetrical vortices correspond to low drag and fluctuating lift, their occurrence in the finite-length cylinder wake contributes to the lower C_D and C_L', compared with those on a two-dimensional cylinder.

(*c*) The maximum longitudinal extent of the reverse flow zone occurs near the mid-span and is significantly larger than in a two-dimensional cylinder wake. This zone contracts when approaching the wall and the cylinder free end, under the influence of upwash and downwash flows. The high three dimensionality of the flow leads to a drop in the normalized vortex shedding frequency to about 0.11 for $H/d = 3 \sim 7$, compared with the two-dimensional wake.

(*d*) The flow depends strongly on the H/d ratio even though the overall flow structure (figure 11) does not. The maximum longitudinal length of the reverse flow zone varies little from $H/d = 1$ to 3, but climbs rapidly from $H/d = 3$ to 7 and then reduces gradually to its minimum at $H/d \rightarrow \infty$ (a two-dimensional cylinder). Both the free-end downwash and upwash flows are enhanced gradually with increasing H/d for the examined H/d range. So do both tip and base vortices. While the base vortex decays monotonically from $x^* = 1$–5, the tip vortex grows from $x^* = 1$–3 and then decays with further increasing x^*.

Y. Zhou wishes to acknowledge support given to him from Research Grants Council of HKSAR through grant PolyU 5334/06E and from The Hong Kong Polytechnic University through grant G-YF30. The authors acknowledge gratefully the fruitful discussion with Professor J. Mi at Peking University in the preparation of this paper.

REFERENCES

Adaramola, M. S., Akinlade, O. G., Sumner, D., Bergstrom, D. J. & Schenstead, A. J. 2006 Turbulent wake of a finite circular cylinder of small aspect ratio. *J. Fluids Struct.* **22**, 919–928.

Adrian, R. J., Christensen, K. T. & Liu, Z. C. 2000 Analysis and interpretation of instantaneous turbulent velocity fields. *Exp. Fluids* **29**, 275–290.

Afgan, I., Moulinec, C., Prosser, R. & Laurence, D. 2007 Large eddy simulation of turbulent flow for wall mounted cantilever cylinder of aspect ratio 6 and 10. *Intl J. Heat Fluid Flow* **28**, 561–574.

Ayoub, A. & Karamcheti, K. 1982 An experiment on the flow past a finite circular cylinder at high subcritical and supercritical Reynolds numbers. *J. Fluid Mech.* **118**, 1–26.

Baban, F., So, R. M. C. & Ötügen, M. V. 1989 Unsteady forces on circular cylinders in a crossflow. *Exp. Fluids* **7**, 293–302.

Balachandar, S., Mittal, R. & Najjar, F. M. 1997 Properties of the mean recirculation region in wakes of two-dimensional bluff bodies. *J. Fluid Mech.* **351**, 167–199.

Bisset, D. K., Antonia, R. A. & Browne, L. W. B. 1990 Spatial organization of large structures in the turbulent far wake of a cylinder. *J. Fluid Mech.* **218**, 439–461.

Bloor, S. M. 1964 The transition to turbulence in the wake of a circular cylinder. *J. Fluid Mech.* **19**, 290–309.

Chyu, C. & Rockwell, D. 1996 Evolution of patterns of streamwise vorticity in the turbulent near wake of a circular cylinder. *J. Fluid Mech.* **320**, 117–137.

Doligalski, T. L., Smith, C. R. & Walker, J. D. A. 1994 Vortex interactions with walls. *Annu. Rev. Fluid Mech.* **26**, 573–616.

Etzold, F. & Fiedler, H. 1976 The near-wake structure of a cantilevered cylinder in a crossflow. *Z. Flugwiss.* **24**, 77–82.

Farell, C., Carrasquel, S., Güven, O. & Patel, V. C. 1977 Effect of wind tunnel walls on the flow past circular cylinder and cooling tower models. *J. Fluids Engng* **99**, 470–490.

Farivar, D. 1981 Turbulent uniform flow around cylinders of finite length. *AIAA J.* **19**, 275–281.

Fouras, A., Dusting, J. & Hourigan, K. 2007 A simple calibration technique for stereoscopic particle image velocimetry. *Exp. Fluids* **42**, 799–810.

Fouras, A., Jacono, D. L. & Hourigan, K. 2008 Target-free stereo PIV: a novel technique with inherent error estimation and improved accuracy. *Exp. Fluids* **44**, 317–329.

Fox, T. A. & West, G. S. 1993*a* Fluid-induced loading of cantilevered circular cylinder in a low turbulence uniform flow. Part 1. Mean loading with aspect ratios in the range 4 to 30. *J. Fluid Struct.* **7**, 1–14.

Fox, T. A. & West, G. S. 1993*b* Fluid-induced loading of cantilevered circular cylinders in a low turbulence uniform flow. Part 2. Fluctuating loads on a cantilever of aspect ratio **30**. *J Fluid Struct.* **7**, 15–28.

Fröhlich, J. & Rodi, W. 2004 LES of flow around a circular cylinder of finite length. *Intl J. Heat Fluid Flow* **25**, 537–548.

Huang, J. F., Zhou, Y. & Zhou, T. 2006 Three-dimensional wake structure measurement using a modified PIV technique. *Exp. Fluids.* **40**, 884–896.

Hunt, J. C. R., Wray, A. A. & Moin, P. 1998 Eddies, stream and convergence zones in turbulent flow. *Tech. Rep.* Report CTR-S88. Centre for Turbulence Research, NASA Ames Research Centre and Stanford University, California.

Hussein, H. J. & Martinuzzi, R. J. 1996 Energy balance of turbulent flow around a surface mounted cube placed in a channel. *Phys. Fluids* **8**, 764–780.

Jeong, J. & Hussain, F. 1995 On the identification of a vortex. *J. Fluid Mech.* **285**, 69–94.

Johnston, C. R., Clavelle, E. J., Wilson, D. J. & Peck, B. J. 1998 Investigation of the vorticity generated by flow around a finite cylinder. In *Sixth Conference of the CFD Society of Canada*, Quebec City, Canada.

Johnston, C. R. & Wilson, D. J. 1997. A vortex pair model for plume downwash into stack wakes. *Atmos. Environ.* **31**, 13–20.

Kawamura, T., Hiwada, M., Hibino, T., Mabuchi, I. & Kumada, M. 1984 Flow around a finite circular cylinder on a flate plate. *Bull. JSME* **27**, 2142–2150.

Krajnović, S. & Davidson, L. 2002 Large-eddy simulation of the flow around a bluff body. *AIAA J.* **40**, 927–936.

Kunz, R. F., D'Amico, S. W., Vassallo, P. F. & Zaccaria, M. A. 2001 LDV measurement of confined parallel jet mixing. *J. Fluids Engng* **123**, 567–573.

Lighthill, M. J. 1963 In *Laminar Boundary Layers* (ed. L. Rosenhead), pp 48–88. Oxford University Press.

Lin, C., Ho, T. C. & Dey, S. 2008 Characteristics of steady horseshoe vortex system near junction of square cylinder and base plate. *J. Engng Mech.* **134**, 184–197.

Lourenço, L. M., Krothapalli, A., Buchlin, J. M. & Riethmuller, M. L. 1986 A non-invasive experimental technique for the measurement of unsteady velocity and vorticity fields. *AIAA J.* **24**, 1715–1717.

Lyn, D. A., Einav, S. E., Rodi, W. & Park, J. H. 1995 A laser-Doppler velocimetry study of ensemble-averaged characteristics of the turbulent near wake of a square cylinder. *J. Fluid Mech.* **304**, 285–319.

Martinuzzi, R. & Tropea, C. 1993 The flow around surface-mounted, prismatic obstacles placed in a fully developed channel flow. *J. Fluids Engng* **115**, 85–92.

Oertel, H. 1990 Wakes behind bluff bodies. *Annu. Rev. Fluid Mech.* **22**, 539–64.

Okajima, A. 1982 Strouhal numbers of rectangular cylinders. *J. Fluid Mech.* **123**, 379–398.

Okamoto, T. & Sunabashiri, Y. 1992 Vortex shedding from a circular cylinder of finite length placed on a ground plane. *J. Fluids Engng* **114**, 512–521.

Okamoto, T. & Yagita, M. 1973 The experimental investigation on the flow past a circular cylinder of finite length placed normal to the plane surface. *Bull. JSME* **16**, 805–814.

Park, C. W. & Lee, S. J. 2000 Free end effects on the near wake flow structure behind a finite circular cylinder. *J. Wind Engng Ind. Aerodyn.* **88**, 231–246.

Pattenden, R. J., Turnock, S. R. & Zhang, X. 2005 Measurements of the flow over a low-aspect-ratio cylinder mounted on a ground plane. *Exp. Fluids* **39**, 10–21.

Patterson, R. W. 1982 Turbofan forced mixer-nozzle internal flowfield, I-benchmark experimental study. *Tech Rep.* CR-3492. NASA.

Perry, A. E. & Chong, M. S. 1987 A description of eddying motions and flow patterns using critical-point concepts. *Annu. Rev. Fluid Mech.* **19**, 125–155.

Raffel, M., Willert, C. E. & Kompenhans, J. 1998 *Particle Image Velocimetry: A Practical Guide.* Springer Science & Business.

Saha, A. K., Muralidhar, K. & Biswas, K. 2000 Experimental study of flow past a square cylinder at high Reynolds numbers. *Exp. Fluids* **29**, 553–563.

Sahin, B., Ozturk, N. A. & Akilli, H. 2007 Horseshoe vortex system in the vicinity of the vertical cylinder mounted on a flat plate. *Flow Meas. Instrum.* **18**, 57–68.

Sakamoto, H. & Arie, M. 1983 Vortex shedding from a rectangular prism and a circular cylinder placed vertically in a turbulent boundary layer. *J. Fluid Mech.* **126**, 147–165.

Sakamoto, H. & Oiwake, S. 1984 Fluctuating forces on a rectangular prism and a circular cylinder placed vertically in a turbulent boundary layer. *J. Fluids Engng* **106**, 160–166.

Sarode, R. S., Gai, S. L. & Ramesh, C. K. 1981 Flow around circular- and square-section models of finite height in a turbulent shear flow. *J. Wind Engng Ind. Aerodyn.* **8**, 223–230.

Simpson, R. L. 2001 Junction flow. *Annu. Rev. Fluid Mech.* **33**, 415–443.

Snyder, W. H. & Lawson, R. E. 1994 Wind-tunnel measurements of flow fields in the vicinity of buildings. In *Eighth Joint Conference on Applications of Air Pollution Meteorology with A&WMA*, Nashville, Tennessee.

Summer, D., Heseltine, J. L. & Dansereau, O. J. P. 2004 Wake structure of a finite circular cylinder of small aspect ratio. *Exp. Fluids* **37**, 720–730.

Tanaka, S. & Murata, S. 1999 An investigation of the wake structure and aerodynamic characteristics of a finite circular cylinder. *JSME Intl J. Ser. B*: *Fluids Therm. Engng* **42**, 178–187.

Wang, H. F., Zhou, Y. & Chan, C. K. 2005 Flow around a finite length square prism.' In *Proceedings of the Fourth European and African Conference on Wind Engineering Institute of Theoretical and Applied Mechanics*, Academy of Sciences of the Czech Republic, Prague.

Wang, H. F., Zhou, Y., Chan, C. K. & Lam, K. S. 2006 Effect of initial conditions on interaction between a boundary layer and a wall-mounted finite-length-cylinder wake. *Phys. Fluids* **18**, 065106.

Wei, T. & Smith, C. R. 1986 Secondary vortices in the wake of circular cylinder. *J. Fluid Mech.* **169**, 513–533.

Williamson, C. H. K. 1988 Defining a universal and continuous Strouhal–Reynolds number relationship for the laminar vortex shedding of a circular cylinder. *Phys. Fluids* **31**, 2742–2744.

Williamson, C. H. K. 1996 Vortex dynamics in the cylinder wake. *Annu. Rev. Fluid Mech.* **28**, 477–539.

Wu, J., Sheridan, J., Welsh, M. C. & Hourigan, K. 1996 Three-dimensional vortex structures in a cylinder wake. *J. Fluid Mech.* **312**, 201–222.

Wu, J., Sheridan, J., Welsh, M. C., Hourigan, K. & Thompson, M. 1994 Longitudinal vortex structures in a cylinder wake. *Phys. Fluids* **6**, 2883–2885.

Zdravkovich, M. M. 1997 *Flow around circular cylinders, vol 1: Fundamentals.* Oxford University Press.

Zdravkovich, M. M. 2003 *Flow around circular cylinders, vol 2: Applications.* Oxford University Press.

Zhong, J. L., Huang, T. S. & Adrian, R. J. 1998 Extracting three-dimensional vortices in turbulent fluid flow. *Pattern Anal. Mach. Intell.* **20**, 193–199.

Zhou, Y. & Antonia, R. A. 1993 A study of turbulent vortices in the wake of a cylinder. *J. Fluid Mech.* **253**, 643–661.

Zhou, Y. & Antonia, R. A. 1994 Critical points in a turbulent near wake. *J. Fluid Mech.* **275**, 59–81.

Zhou, Y., Zhang, H. J. & Yiu, M. W. 2002 The turbulent wake of two side-by-side circular cylinders. *J. Fluid Mech.* **458**, 303–332.